

STRICT UPPER LIMITS ON THE CARBON-TO-OXYGEN RATIOS OF EIGHT HOT JUPITERS FROM SELF-CONSISTENT ATMOSPHERIC RETRIEVAL

BJÖRN BENNEKE

Division of Geological and Planetary Sciences, California Institute of Technology, Pasadena, CA 91125, USA

Abstract

The elemental compositions of hot Jupiters are informative relics of planet formation that can help us answer long-standing questions regarding the origin and formation of giant planets. Here, I present the main conclusions from a comprehensive atmospheric retrieval survey of eight hot Jupiters with detectable molecular absorption in their near-infrared transmission spectra. I analyze the eight transmission spectra using the newly-developed, self-consistent atmospheric retrieval framework, SCARLET. Unlike previous methods, SCARLET combines the physical and chemical consistency of complex atmospheric models with the statistical treatment of observational uncertainties known from atmospheric retrieval techniques. I find that all eight hot Jupiters consistently require carbon-to-oxygen ratios (C/O) below ~ 0.9 . The finding of $C/O < 0.9$ is highly robust for HD 209458b, WASP-12b, WASP-19b, HAT-P-1b, and XO-1b. For HD 189733b, WASP-17b, and WASP-43b, I find that the published *WFC3* transmission spectra favor $C/O < 0.9$ at greater than 95% confidence. I further show that the water abundances on all eight hot Jupiters are consistent with solar composition. The relatively small depth of the detected water absorption features is due to the presence of clouds, not due to a low water abundance as previously suggested for HD209458b. The presence of a thick cloud deck is inferred for HD 209458b and WASP-12b. HD 189733b may host a similar cloud deck, rather than the previously suggested Rayleigh hazes, if star spots affect the observed spectrum. The approach taken in SCARLET can be regarded as a new pathway to interpreting spectral observations of planetary atmospheres. In this work, including our prior knowledge of H-C-N-O chemistry enables me to constrain the C/O ratio without detecting a single carbon-bearing molecule.

1. INTRODUCTION

Spectroscopy observations of hot Jupiters provide an unprecedented opportunity to constrain the metallicities and carbon-to-oxygen ratios (C/O) of giant planets which can provide crucial hints on the formation of giant planets including the gas and ice giants in our solar system. If giant planets predominately form in a quick one-step process through gravitational instability (Boss 1997), their atmospheres should have elemental abundances resembling the ones of their host star (Helled & Schubert 2009). If, on the other hand, giant planets form through multi-step core accretion process (Pollack et al. 1996), a wide range of elemental compositions with distinct deviations from the host star's elemental composition are expected (Öberg et al. 2011; Helling et al. 2014; Madhusudhan et al. 2014a; Ali-Dib et al. 2014; Mordasini et al., 2015). Within the core accretion model, refractory and ice-forming elements first segregate from the gas in the protoplanetary disk through condensation. They then evolve separately from the gas for millions of years, and finally, some of the gas and solids are recombined in the process of planet formation. In this multi-step process, it would be a strange coincidence for the final planet to form with elemental compositions identical to the one of the host star. Instead, we expect the elemental abundances of giant exoplanets to be insightful relics of this planet formation process.

The carbon-to-oxygen ratio (C/O), in particular, has been proposed to be a good tracer of planet formation. Protoplanetary disk models suggest that the C/O ratio of the gas and solids in protoplanetary disks varies

with distance from the star because of the different condensation temperatures of H₂O and CO (Öberg et al. 2011). Detailed disk evolution models suggest that the C/O of the gas beyond the water iceline should transition to $C/O \rightarrow 1$ on time scales of ~ 3 Myrs (Helling et al. 2014). As a result, the gas envelopes of giant planets formed beyond the iceline may be carbon enriched with the exact C to O ratio depending on the time and the location of the runaway gas accretion. If, on the other hand, gas giant atmospheres are heavily polluted by the accretion of oxygen enriched solids, the C/O ratio of giant planet envelopes may substantially deviate from the C/O ratio in the gas disk. Van Boekel et al. (2015) model the formation and evolution of giant exoplanets from the formation of planetesimals to today's evolved giant planets, keeping track of the amounts of gaseous, icy, and rocky material accreted as the planets forms and migrates within the disk. They conclude that giant planet formation beyond the water ice line should always lead to $C/O < 1$, while giant planet formation within the iceline can lead to either carbon-rich chemistry ($C/O > 1$) or oxygen-rich chemistry ($C/O < 1$) depending on the carbon abundance of refractory materials. The uncertainties in planet formation and disk evolution models are substantial, however. Observational constraints on the elemental abundances of giant planets are greatly needed.

The challenge in obtaining reliable observational constraints on the elemental abundances lies not only in obtaining sufficiently precise data, but also in the difficulty associated with inferring elemental abundances representative of the planet's bulk gas envelope from spectroscopic observations of the planet's photosphere. Despite

exquisite observations, no representative values for the C/O ratios of the solar system gas giants, no representative values for the C/O ratio in the Solar System giants have been determined to date, because oxygen is condensed out in the form of water in deep layers, largely inaccessible to remote sensing. More accurate oxygen abundances and C/O ratios for the solar system gas giants would provide an important new constraint on our models of gas giant planet formation. One of the main science objectives of the Juno mission — expected to arrive in 2016 — is to provide the first representative C/O measurement for Jupiter’s gas envelope through microwave observations from a low Jupiter orbit.

Observations of hot Jupiters and directly imaged young giant planets present a new opportunity to determine the elemental abundances for a large sample of giant planets using infrared spectroscopy. The temperatures in their atmospheres are sufficiently high that all of the dominant carbon or oxygen bearing molecular species are accessible to IR remote sensing. However, the spectral signatures of exoplanets are governed not only by the planet’s elemental composition, but also its radiation environment and a wide range of weakly understood chemical and dynamical processes in their atmosphere.

Here, I introduce a new “Self-Consistent Atmospheric Retrieval framework for Exoplanets” (SCARLET) which aims to provide direct constraints on elemental abundances while accounting for the uncertainties resulting from our limited understanding of the chemical, dynamical and cloud formation processes in the atmospheres of these planets. Unlike previous methods, the new framework is able to determine the full range of self-consistent scenarios for a given planet by combining the observational data and our prior knowledge of atmospheric chemistry and physics in a statistically robust Bayesian analysis. One key concept is that for a given metallicity and C/O ratio there is not a single model transmission spectrum to be compared to the data, but instead a range of models corresponding to the uncertainties introduced by our limited understanding of the relevant atmospheric processes. SCARLET accounts for this model uncertainty by marginalizing over a wide range of “atmospheric process parameters” whose prior distributions quantify our limited knowledge of vertical mixing, chemistry, and cloud formation in the atmospheres of hot exoplanets.

In this first work, I apply the SCARLET framework to eight published hot Jupiter transmission spectra with detectable near-IR molecular absorption features (HD 209458b, WASP-19b, HAT-P-1b, XO-1b, HD 189733b, WASP-12b, WASP-17b, and WASP-43b). In this study, we focus on *HST WFC3* observations because they provide substantial *simultaneous* spectral coverage (1.1 – 1.7 μm), and have been shown to be extremely repeatable (e.g., Kreidberg et al. 2014a), leaving little doubt about the reliability of the water detections. Where available we include *HST STIS* and *Spitzer* observations in the analysis — note, however, that the C/O constraints presented in this work rely only on the *HST WFC3* observations. Our primary conclusions do not depend on comparisons of observations taken at different times, and the repeatability of *WFC3* observations strongly indicates that the results are not compromised by systematic effects that may have affected early C/O

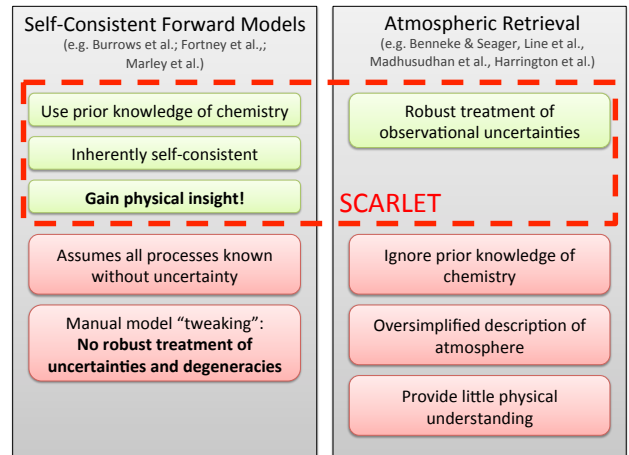


FIG. 1.— Strength and weakness of self-consistent forward models and atmospheric retrieval techniques for the interpretation of exoplanet spectra. Strengths are marked in green. Weakness are marked in red. The new “SCARLET” approach combines the strengths of self-consistent forward modeling and atmospheric retrieval techniques and overcomes their weaknesses.

measurements based on broadband *Spitzer IRAC* data points (e.g., Madhusudhan et al. 2011; Crossfield et al. 2012a; Cowan et al. 2012).

In this article, I first motivate the development of the new SCARLET framework by reviewing the strengths and weaknesses of previous modeling approaches for analyzing planetary atmospheres (Section 2). Section 3 then describes the details of the SCARLET framework. Section 4 describes the results from the retrieval study of four hot Jupiters. Section 5 presents the conclusions from this work and discusses the implications for hot Jupiter formation and migration.

2. BACKGROUND: INTERPRETING PLANETARY SPECTRA

The interpretation of spectral observations of solar system atmospheres, exoplanets, and brown dwarfs has historically been performed using two distinct modeling strategies: “Atmosphere forward modeling” is a theory-driven approach in which the governing equations of chemistry and physics are solved to derive a small number of self-consistent scenarios for the atmosphere. “Atmospheric retrieval”, on the other hand, is an observation-driven approach in which statistically robust constraints on the atmospheric state molecular composition and temperature structure are retrieved by repeatedly comparing observations to model spectra of parameterized scenarios without modeling the chemical and physical process in the atmosphere. Both approaches have strengths and severe limitations (Figure 1). The goal of this section is to provide a concise overview of “forward models” and “atmospheric retrieval techniques” to motivate the development of the new SCARLET framework presented in this work.

2.1. Complex Atmospheric “Forward” Models

The basic idea of atmosphere forward models is to iterate the relevant atmospheric processes including atmospheric chemistry, radiative-convective heat transport, and/or cloud formation until a converged self-consistent solution is achieved (Burrows et al. 1997; Seager & Sas-

selov 2000; Fortney et al. 2008; Showman et al. 2009; Menou 2013). Depending on the application, particular emphasis is assigned on modeling the detailed chemistry (e.g., Zahnle et al. 2009; Moses et al. 2011a; Hu et al. 2012), the atmospheric dynamics (e.g., Showman et al. 2009), the thermal structure (e.g., McKay et al. 1989; Burrows et al. 1997; Fortney et al. 2011) and/or the formation of clouds (e.g., Marley et al. 2002; Lavvas et al. 2010; Morley et al. 2013). The main strength of these atmosphere “forward” models is that they provide physical insights into the atmospheric processes at play. Matching the observations generally requires modeling all relevant physical processes. If solved iteratively, atmospheric scenarios from atmosphere forward models are generally physically self-consistent within the modeled physics.

Severe limitations of atmosphere “forward” modeling are, however, that they inherently assume that all physical and chemical processes are known without uncertainty (Figure 1). Mismatch between data and models is often reduced by manually tweaking individual model parameters until a sufficient match to the data is achieved. Manual tweaking, however, prevents a statistically robust treatment of the observational uncertainty. Individual scenarios matching the data are identified without understanding what the degeneracies are and whether the found scenario is the only plausible scenario.

2.2. Atmospheric Retrieval

Atmospheric retrieval methods are different from atmosphere “forward” models in that they generally do not model any of the chemical and dynamical processes in the atmosphere. Instead, they describe the molecular composition and temperature profile by free parameters and model the planet’s spectrum for comparison to the data. Atmospheric techniques are powerful when good data is available and have a long history of applications in meteorology (e.g. Smith 1970; Chahine 1974) and the exploration of the solar system planets (e.g., Hanel et al. 2003). An excellent overview of the theory of atmospheric retrieval within the assumptions of Gaussian uncertainties is provided in Rodgers (2000). Techniques that more robustly explore the full parameter space of planetary atmospheres are described in Madhusudhan & Seager (2009); Benneke & Seager (2012); Line et al. (2012).

A key disadvantages of atmospheric retrieval techniques is that they provide no direct insights into the physical and chemical processes at play. They also make no use of our prior substantial knowledge of atmospheric chemistry and heat transport to better constrain the properties of the planet studied. This is particularly critical for exoplanets because the available data is sparse and including our prior knowledge of chemistry or heat transport can substantially reduce the uncertainties in the inferred elemental abundances and internal heat flux. Instead, atmospheric retrieval techniques make no attempt to rule out unphysical scenarios that grossly contradict our basic understanding of atmospheric chemistry and radiative-convective heat transport. Combinations of molecular gases that are highly reactive with each other at given conditions are not ruled out in regular retrieval methods (see Hu & Seager 2014 for a discussion). Similarly, no consistency check between the parameterized temperature-pressure profile and the molecular composition is performed (Madhusudhan & Seager 2009; Line

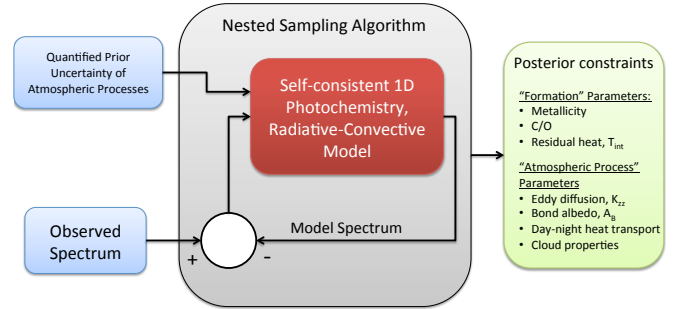


FIG. 2.— Schematic view of the SCARLET framework.

et al. 2013a)). Equally important, atmospheric retrieval techniques for exoplanets require an oversimplified description of atmosphere in order to reduce the number of free parameters. Well-mixed atmospheres composed of only a small number of pre-selected molecules are considered, even though the mixing ratios realistic atmospheres can be strongly altitude dependent (Moses et al. 2013b,a). The presented shortcoming of atmospheric retrieval techniques suggest the potential for an improved way to analyze spectroscopic observations of exoplanets — one that combines the statistical robustness of atmospheric retrieval techniques with the physical insights provided by atmosphere forward models.

3. METHODOLOGY: THE SCARLET FRAMEWORK

The main objective of the SCARLET framework is to determine the full range of self-consistent scenarios for an observed planet by combining the observational data and our prior knowledge of atmospheric chemistry and physics in a statistically robust Bayesian analysis. SCARLET consists of a state-of-the-art self-consistent photochemistry model surrounded by the nested sampling algorithm for the retrieval. This architecture enables SCARLET to provide direct insights into the elemental composition of the deep atmosphere and planetary bulk based on spectral observations of the upper atmosphere. Compared to previous modeling approaches, SCARLET combines the statistical robustness and exploratory nature of traditional atmospheric retrieval methods (Smith et al., 1970; Rodgers et al. 2000; Madhusudhan & Seager 2009; Benneke & Seager 2012) with the self-consistency and ability to provide physical insights of so-called self-consistent atmospheric forward models (e.g., Burrows et al. 1997, 2001; Marley et al. 2002; Fortney et al. 2008, 2011; Moses et al 2013).

SCARLET is distinct from any previous atmospheric retrieval methods that describe the current state of the visible atmosphere (molecular abundance and temperature profiles) by free parameters. The advantage of the SCARLET approach are as follows: (1) SCARLET provides direct insight into the elemental composition of the planet’s deep atmosphere, (2) all atmospheric scenarios found by SCARLET are inherently self-consistent (within the limits of our prior knowledge of atmospheric chemistry and physics), (3) SCARLET can provide direct constraints on physical processes such as the strength of vertical mixing in the studied atmospheres.

3.1. SCARLET Overview

Figure 2 illustrates the basic architecture of the SCARLET framework. The input to the framework are the

TABLE 1
 “FORMATION” PARAMETERS (TOP) AND “ATMOSPHERIC PROCESS”
 PARAMETERS (BOTTOM) AND THEIR PRIOR RANGES IN THE SCARLET
 RETRIEVAL ANALYSIS

SCARLET	Prior range
Metallicity at 1000 bar	0.1 ... 100
C/O at 1000 bar	0.0001 ... 10000
Internal heat	0 ... 200 K
Eddy diffusion coefficient, K_{zz}	$10^7 \dots 10^{11} \text{ cm}^2 \text{ s}^{-1}$
Bond albedo	0 ... 0.9
Dayside-nightside heat redistribution factor	0.25 ... 0.5
Cloud properties	see Section 3.3.3

observed planetary spectrum and an explicit, quantitative description of our prior knowledge of atmospheric chemistry and physics. The framework then repeatedly runs a self-consistent atmospheric chemistry and radiative-convective model to systemically explore atmospheric scenarios to derive posterior constraints on the underlying elemental composition of the planet’s gas envelope and the strength and efficiencies of process at play in the atmosphere.

3.2. Planet Parameterization

The fundamental idea of SCARLET is to divide all unknown properties of the planet into “formation history” parameters and “atmospheric process” parameters. Formation history parameters describe properties of the planet that are set by the planet’s formation and evolution history, such as its elemental composition and residual accretion heat. Atmospheric process parameters describe the strengths or efficiencies of *ongoing* chemical and physical processes in the atmosphere.

3.2.1. “Formation History” Parameters

One of the main goals of studying exoplanets is understanding the formation and evolution history of planets. Planet properties that provide hints on the planet’s formation histories are the bulk elemental composition of the planet’s gas envelope and the residual interior accretion heat. While spectroscopic observations of exoplanets cannot probe these properties directly, SCARLET models the chemistry, radiative transfer, and mass and heat exchange between the observable optically-thin atmosphere and the planet deep atmosphere in order to derive conclusion on the formation history parameters based on spectroscopic observations of the planet.

Elemental Composition— In this work, I parameterize the elemental composition of the deep atmosphere by the metallicity (M) and carbon-to-oxygen ratio (C/O) at the 1000 bar level. The metallicity is defined as

$$M = \frac{[X/H]}{[X/H]_{\text{Solar}}}, \quad (1)$$

where H is the abundance of hydrogen by number and X is abundance of any element heavier than helium. A metallicity of 10 times solar ($M = 10$) and the fiducial $C/O = (C/O)_{\text{Solar}} = 0.54$ means that all elements heavier than Helium are ten times more abundant than they are in the Sun. A log-uniform prior is assigned for metallicities between 0.1 and 100 (Table 1). The helium to hydrogen ratio is assumed to be equal to the solar value.

The C/O parameter additionally allows for variations in relative abundances of carbon and oxygen, while keeping the sum of the mixing ratios of carbon and oxygen constant. C/O ratios between 10^{-5} (100,000 times more C) and 10^5 (100,000 times more O) are explored. A custom-made stretching is applied to ensure an effective exploration of the parameter space between $C/O = 0.1$ and $C/O = 10$, where most of the changes in chemistry take place (see y-axis in Figure 8). A uniform prior probability is applied in the stretched parameter space, correctly reflecting our prior understanding that scenarios with extreme C/O ratios are less likely than C/O ratios between 0.1 and 10.

Interior heat— The interior heat is described by the effective internal temperature,

$$T_{\text{int}} = \left(\frac{F_{\text{Total}}}{4\pi\sigma R_P^2} \right)^{1/4}, \quad (2)$$

where F_{Total} is the total cooling power of the planet interior, $4\pi R_P^2$ is the planet’s surface area at the top of the atmosphere, and σ is the Stefan–Boltzmann constant. A uniform prior on the log scale is between 0 K and 200 K.

3.2.2. “Atmospheric Process” Parameters

The atmospheric process parameters describe chemical and physical processes in the atmosphere that are weakly understood a priori, but highly relevant for the interpretation of the observed spectrum. In this work, the atmospheric process parameters include the eddy diffusion coefficient (K_{zz}), the properties of clouds, the dayside-nightside heat transport. Atmospheric process parameters are essential for constraining the desired elemental composition because they provide the connection between the desired elemental compositions and the observable near-infrared spectrum of the studied hot Jupiters and enable me to account for our uncertain prior knowledge of atmospheric processes.

Eddy diffusion— The eddy diffusion coefficient (K_{zz}) is an essential free parameter because the vertical transport of atmospheric constituents in hot Jupiter atmosphere is weakly understood and it sensitively affects how closely the observable upper atmosphere of the planet resembles the composition in the deep atmosphere. UV photons from the star break up molecular bonds in the upper atmosphere, thereby significantly reducing the molecular abundances of species such as methane and water vapor in the upper atmosphere. The level to which their abundances are reduced depends sensitively on the vertical transport of atmospheric constituents that continuously replenish these abundances. Deriving constraints on the bulk elemental composition of the gas envelope from molecular absorption formed in the upper atmosphere, therefore, requires me to account for the uncertainty introduced by the unknown eddy diffusion coefficient. For hot Jupiters, eddy diffusion coefficients are uncertain over several orders of magnitude for hot Jupiters ($K_{zz} = 10^7 - 10^{10} \text{ cm}^2 \text{ s}^{-1}$).

Heat redistribution— The dayside-nightside heat redistribution is parameterized through a factor, f , that relates

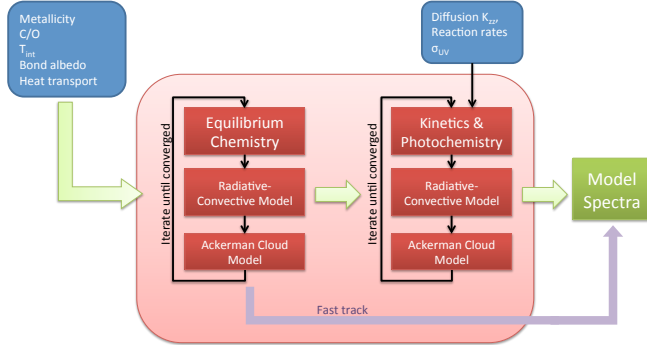


FIG. 3.— Flow chart of the self-consistent photochemistry-thermochemistry model applied in SCARLET.

the irradiation of the 1D model atmosphere to the stellar flux at the planet’s orbital distance from its host star. The extreme limits are full heat redistribution, i.e. the incoming radiation is uniformly distributed across the planet, and no dayside-nightside heat transport, i.e. all the radiation is deposited on the planet’s dayside. The heat redistribution factor ranges from $f = 0.25$ for efficient heat redistribution to $f = 0.5$ for no dayside-nightside heat transport.

Clouds— Two different cloud modeling approaches are considered in this work. The “parameterized particle size and cloud profile” model captures the wide range of cloud effects in exoplanet transmission spectra through four parameters describing the effective grain size (r_{eff}), the cloud top pressure (p_{top}), the condensate mole fraction (q_*), and a cloud profile shape factor (H_c). Alternatively, a simplified, two-parameter “Gray Clouds + Rayleigh hazes” model describes the clouds in the atmospheres by specifying the cloud top pressure of a gray cloud deck and the additional Rayleigh-like opacity due to small particles. The details of the both cloud modeling approaches are discussed in Section 3.3.3.

3.3. Self-Consistent Photochemistry-Thermochemistry Model

The objective of the photochemistry-thermochemistry model is to compute self-consistent model atmospheres and synthetic planetary spectra for any plausible elemental composition, internal heat flux, stellar irradiation, and atmospheric process parameters. Self-consistent molecular compositions and temperature structures are obtained by iteratively solving atmospheric chemistry, radiative-convective heat transport, and hydrostatic equilibrium. A unique feature of the model is that, in its most sophisticated form, it self-consistently solves the atmospheric chemistry via a full thermo- and photochemical kinetics and transport model and the radiative-convection heat transport via a high-resolution, line-by-line radiative transfer scheme (Figure 3). This approach enables the derivation of self-consistent molecular compositions and temperature structures for any plausible elemental composition. The model complexity can be reduced by approximating the composition through computationally efficient thermal equilibrium calculations.

3.3.1. Chemical Models

Two chemical models with different levels of sophistication are used in this work. The low-complexity model

is a chemical equilibrium model minimizing Gibb’s free energy in each layer of the atmosphere; the high complexity model is a full thermo- and photochemical kinetics and transport model. Both models were specifically designed to maximize computational efficiency to enable thousand of evaluations necessary for the parameter exploration in SCARLET. The advantage of the chemical equilibrium model is its computational efficiency. Chemical equilibrium abundances can be computed $\gtrsim 10^3$ times faster than performing a full evaluation of the thermo- and photochemical kinetics and transport model. Inferring the elemental abundance of the deep atmosphere based on the observable upper atmosphere, however, requires capturing transport-induced quenching in the mid-atmosphere, and photochemistry in the upper atmosphere, which can only be captured by a full thermo- and photochemical kinetics and transport model.

Equilibrium chemistry model— The low-complexity equilibrium chemistry model computes the molecular compositions from the elemental abundances by minimizing Gibb’s free energy in each layer of the atmosphere (White et al., 1958; Miller-Ricci et al. 2009; Benneke & Seager 2013). I consider approximately 200 molecular species from the elements H, He, C, N, O, Ne, Na, Mg, Al, Si, P, S, Cl, Ar, K, Ca, Ti, Cr, Mn, Fe, and Ni. Rapid computation of $\sim 10^5$ molecular compositions is accomplished by interpolating the molecular abundance for each species from a precomputed 4-dimensional equilibrium grid (30x30x60x30) spanning the dimensions atmospheric metallicity, C/O ratio, pressure, and temperature.

Kinetics and transport model— The thermo- and photochemical kinetics and transport model computes the molecular composition of the atmosphere by solving the coupled mass-continuity equations as a function of pressure for each molecular species:

$$\frac{\partial n_i}{\partial t} + \frac{\partial \Phi_i}{\partial z} = P_i - L_i, \quad (3)$$

where n_i is the number density of species i (m^{-3}), Φ_i is the vertical transport flux of species i ($\text{m}^{-2}\text{s}^{-1}$), P_i is the chemical production rate ($\text{m}^{-3}\text{s}^{-1}$), and L_i is the chemical loss rate ($\text{m}^{-3}\text{s}^{-1}$), and z is the vertical coordinate in the atmosphere (m). The chemical production and loss rates are computed by summing the contributions of 1760 chemical reactions given the molecular abundance, pressure, temperature in each layer. The vertical transport flux includes eddy diffusion and molecular diffusion

$$\Phi_i = -K_{zz}N \frac{\partial f_i}{\partial z} - DN \frac{\partial f_i}{\partial z} + Dn \left(\frac{1}{H_0} + \frac{1}{H_i} + \frac{\alpha_T}{T} \frac{dT}{dz} \right), \quad (4)$$

where K_{zz} is the parameterized eddy diffusion coefficient, N is the total number density, $f_i \equiv n_i/N$ is the mixing ratio, D is the molecular diffusion coefficient, H_0 is the mean scale height, H_i is the scale height of species i , and α_T is the thermal diffusion factor.

The kinetics and transport model, in principle, fully captures the three main chemical processes in planetary atmospheres—thermochemical equilibrium in the deep atmosphere, transport-induced quenching in the

mid-atmosphere, and photochemistry in the upper atmosphere. A state-of-the-art reaction list of 1760 chemical reactions for 92 molecular species formed by the elements H, C, O, and N is adopted from Moses et al. (2013a). Thermochemical equilibrium is recovered at high pressure and temperature because the chemical reaction list includes a matching reverse reaction for each chemical reaction (Visscher & Moses 2011).

For the boundary conditions, I assume a zero-flux condition at the top of the atmosphere boundary and impose the chemical equilibrium abundances for the specified elemental abundance of the planet’s gas envelope at the lower boundary. The use of a zero-flux condition at the upper boundary assumes that the atmospheric loss is negligible; Moses et al. (2011) discuss this assumption in detail and show that it has no effect on the atmospheric composition in the photosphere. The lower boundary is set at 1000 bar where temperatures are above 2500 K such that chemical equilibrium mixing ratios will prevail. The purpose of SCARLET framework is to constrain the elemental abundances at the lower boundary, i.e. the boundary conditions to the kinetics and transport model, based on observations of the upper atmosphere. At the top of the atmosphere, the computational domain reaches to 10^{-10} bar; this is sufficiently high to capture the UV dissociation of all major molecular species. The effect of the zero-flux condition at the upper boundary neglects atmospheric loss; thoroughly discussed in Moses et al. (2011a), showing that neglecting atmospheric loss has no effect on the stratospheric or lower-thermospheric results.

Equations 3 and 4 form a stiff system of 9200 coupled differential equations for a 100 layer atmosphere, presenting a substantial computational challenge. The stiffness of the system results from the vastly different reaction times scales of the modeled reactions. To efficiently solve the stiff system, I use a quasi-constant step-size implementation of the Numerical Differentiation Equation (NDFs). NDFs are found to be more efficient for chemical kinetics problems as compared with inverse Euler methods generally used in state-of-the-art atmospheric chemistry codes (Allen et al. 1981; Zahnle et al. 2009; Hu et al. 2012; Moses et al. 2013a). Additional acceleration of the computation is accomplished by recomputing the Jacobian matrix only when it has substantially changed (Brown et al. 1989). Despite these improvements, the use of the full the full kinetics and transport model remains the primary bottleneck for SCARLET retrieval runs. Evaluation of the kinetics and transport model are initialized with a converged solution from iterating the chemical equilibrium and radiative convective model (Figure 3).

3.3.2. Line-by-Line Radiative-Convective Model

The purpose of the radiative-convective model is to compute temperature-pressure profiles self-consistent with the stellar insolation and molecular composition of the atmosphere (Section 3.3.1). To accomplish this, the radiative-convective model iterates the T - p profile until the radiative downward flux F^\downarrow due to direct star light and infrared reemission is matched by the upward emission flux in the atmosphere F^\uparrow . In the process, atmospheric layers with temperature gradients exceeding the adiabatic lapse rate $-\frac{dT}{dz} > \Gamma = \frac{g}{C_p}$ are declared convec-

tive and adjusted to the adiabatic lapse rate.

Converging to radiative-convective equilibrium can require hundreds of radiative transfer calculations of the entire atmospheric column. In this work, I present a novel numerical technique to speed up repeated line-by-line radiative transfer calculations by orders of magnitudes (Appendix A). The new numerical technique enables the efficient computation of self-consistent T-p profiles for any molecular composition based on line-by-line equivalent radiative transfer. Line-by-line radiative transfer has the advantage that it accurately describes the radiative transport for any atmospheric composition, while analytical solution for (semi-)gray opacities can deviate significantly from the exact solution (e.g., Parmentier & Guillot 2014) and the assumption of correlated opacities across the entire atmospheric column can also become problematic, in particular for atmospheres with temperature-pressure profiles near the CH_4/CO or N_2/NH_3 transition for which the mixing ratios of dominant absorbers can be strongly altitude-dependent.

3.3.3. Cloud Models

Clouds play a dominant role in shaping the observable transmission spectra of exoplanets, yet the formation and chemistry of clouds on exoplanets are poorly understood. As a result, clouds present a substantial uncertainty in retrieving the desired atmospheric composition of exoplanets. Given the lack of a reliable predictive model for clouds on exoplanets, the approach taken in SCARLET is to describe the clouds properties using free parameters with the goal of capturing the full range of plausible cloud properties. Marginalizing over the cloud properties allows us to determine robust constraints on the planet’s gas envelope composition while accounting for our limited prior understanding of cloud formation. Two cloud parameterization are applied in this work:

“Parameterized Cloud Profile and Particle Size” Model—The “parameterized particle size and cloud profile” model captures a broad range of cloud effects in exoplanet transmission spectra by exploring different cloud compositions and describing the particle size and vertical cloud density profile via free parameters in the fit. Capturing the uppermost structure of the clouds is particularly important because transmission spectroscopy probes relatively low pressures as starlight travels on a slant path through the planet’s upper atmosphere (Fortney & Marley 2005)

The approach taken here is to describe the vertical cloud density profile of the uppermost clouds or hazes by

$$q_c(p) = q_* (\log p - \log p_{\text{top}})^{H_C} \quad \text{for } p_{\text{top}} \leq p < p_{\text{base}} \quad (5)$$

where $q_c \equiv n_{\text{Cond}}/n_{\text{H}_2}$ is the condensate mole fraction at pressure p , H_C is the cloud profile shape factor, p_{top} is the cloud top pressure, p_{base} is the pressure at the cloud base, and q_* is the condensate mole fraction one scale height below the cloud top (Figure 4). The functional form of Equation 5 is chosen to resemble cloud profiles observed and modeled for the solar system and brown dwarfs. The particle size distribution is described by a log-normal distribution

$$n(r) = \frac{1}{\sqrt{2\pi r \log \sigma}} e^{-\frac{(\log r - \log r_{\text{eff}})^2}{2(\log \sigma)^2}}, \quad (6)$$

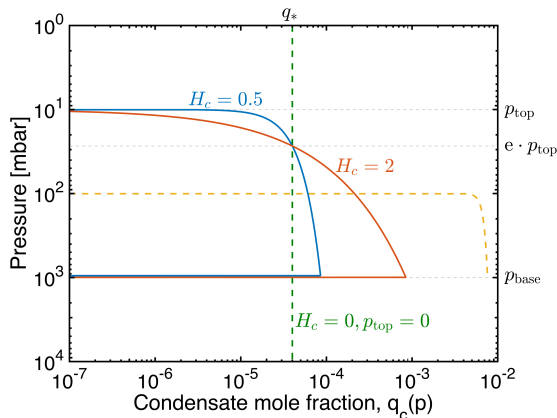


FIG. 4.— Example cloud profiles for the “parameterized cloud profile and particle size” model. The parameterization encompasses a wide range of cloud profiles including cloud profiles resembling the ones of typical condensation clouds (red, blue curves — compare Ackerman & Marley (2001)), cloud profiles that assume a uniform condensate mole fraction (green, dashed line — compare Etangs et al. (2008)), and sharp cloud decks (yellow dashed, Benneke & Seager (2012)). The motivation for parameterizing the clouds through free parameters, rather than modeling them self-consistently, is that our prior knowledge of the nature and formation of clouds on hot Jupiters is generally insufficient to reliably capture even the basic trends in the cloud formation.

where r_{eff} is the parameterized effective particle size and the effective variance is set to $\sigma = 2$. Altogether, parameterized particle size and cloud profile describes the uppermost cloud deck by the four free parameters (q_c , p_c , H_c , and p_{top}). Transmission spectra generally convey little information about the cloud base, thus p_{base} is assumed to be high enough that it has a minimal effect on the transmitted starlight. Marginalization over the wide range of cloud profiles considered in the “parameterized grain size and cloud profile” model ensures that retrieved constraints on the atmospheric composition are largely independent of assumptions on the unknown vertical transport of cloud particles.

Particles composed of MgSiO_3 , MgFeSiO_4 , and SiC are considered for the hot Jupiters studied in this work ($T_{\text{eq}} = 1410 \dots 2010$). The radiative properties are computed using Mie scattering theory (Hansen & Travis 1974) and the complex refractive indices taken from Dorschner et al. (1995).

Gray Clouds + Rayleigh Hazes— Most published observations of exoplanets provide little information to observationally constrain the detailed cloud profiles or grain size. Given sparse data, it can be instructive to investigate the constraints on cloud top pressure and haze opacity from a low-complexity “gray cloud deck + Rayleigh hazes” model. The two-parameter “gray cloud deck + Rayleigh hazes” cloud model simultaneously allows for the presence of a gray cloud deck as well as “Rayleigh” hazes composed of small particles ($r_p \ll \lambda$).

Gray clouds are modeled as a sharp cutoff to the planet-grazing starlight below a parameterized pressure level in the atmosphere. A sharp cutoff approximates the appearance of an upper cloud deck composed on large particle or a sudden increase cloud density. Rayleigh hazes are assumed to be composed of small particles ($r_p \ll \lambda$). The opacity of the particles follows $k \propto k_{0.4} (0.4 \mu\text{m}/\lambda)^{-4}$, where $k_{0.4}$ is the extinction coefficient (cm^2/g) at $0.4 \mu\text{m}$.

3.3.4. Opacities

The radiative transfer calculations in this work include opacities due to molecular absorption, collision-induced broadening from H_2/H_2 and H_2/He collisions (Borysov 2002), Rayleigh scattering (see Benneke & Seager 2012), and Mie scattering of cloud and haze particles. Molecular absorption cross sections are determined directly from the molecular line lists provided in the high-temperature ExoMol database (Tennyson & Yurchenko 2012) for CH_4 , NH_3 , and TiO , HITEMP database (Rothman et al. 2010) for H_2O , CO , and CO_2 , and the HITRAN database (Rothman et al. 2009) for O_2 , O_3 , OH , C_2H_2 , C_2H_4 , C_2H_6 , H_2O_2 , and HO_2 . Absorption by the alkali metals (Li, Na, K, Rb, and Cs) is modeled based on the line strengths provided in the VALD database (Piskunov et al. 1995) and using the H_2 -broadening prescription provided in Burrows & Volobuyev (2003).

To speed up the evaluation of a large number of atmospheric models, I precompute the wavelength-dependent molecular cross sections for each of the considered molecular species on a temperature and log-pressure grid and then interpolate the cross section for the required conditions. Similarly, the scattering properties of Mie scattering of cloud and haze particles are precomputed as a function of particle size and wavelength.

In the upper atmosphere, molecular absorption lines become increasingly narrow, requiring a very high spectral resolution to exactly capture the shapes of the thin Doppler-broadened lines (Goody & Yung 1995). Instead of ensuring that each line shape at low pressure is represented exactly, I choose an appropriate spectral resolution for the line-by-line simulation by ensuring that the simulated observations are not altered by more than 1% of the observational error-bar when the spectral resolution is doubled or quadrupled.

3.3.5. Transmission Spectrum Model

Once the chemistry-radiative convective model has converged to a steady-state solution, I compute model transmission spectra and synthetic instrument outputs to evaluate the fit between the model and the observations. The model computes the absorption and scattering of stellar light by the planetary atmosphere as the rays traverse the day-night terminator region. Extinction due to molecular absorption, Rayleigh scattering, and cloud particles absorption and scattering is accounted for. In the parameterized cloud profile, the optical properties of finite-size cloud particles are computed using Mie scattering theory. In the “gray cloud deck + Rayleigh haze” model, the gray cloud deck is modeled as a sharp cutoff of transmission below the parameterized cloud deck pressure level. Rayleigh hazes are included as an ad-hoc opacity source with $\sigma \propto \lambda^{-4}$. Finally, the high-resolution transmission spectrum is integrated over the instrument response function of the individual instrument channels for comparison to the astronomical observations.

3.4. Nested Sampling for Atmospheric Retrieval

SCARLET employs the multimodal nested sampling algorithm, MultiNest, to efficiently explore the multidimensional parameter space and compute the posterior distribution of the formation and atmospheric process parameters. The mathematical details of the nested sam-

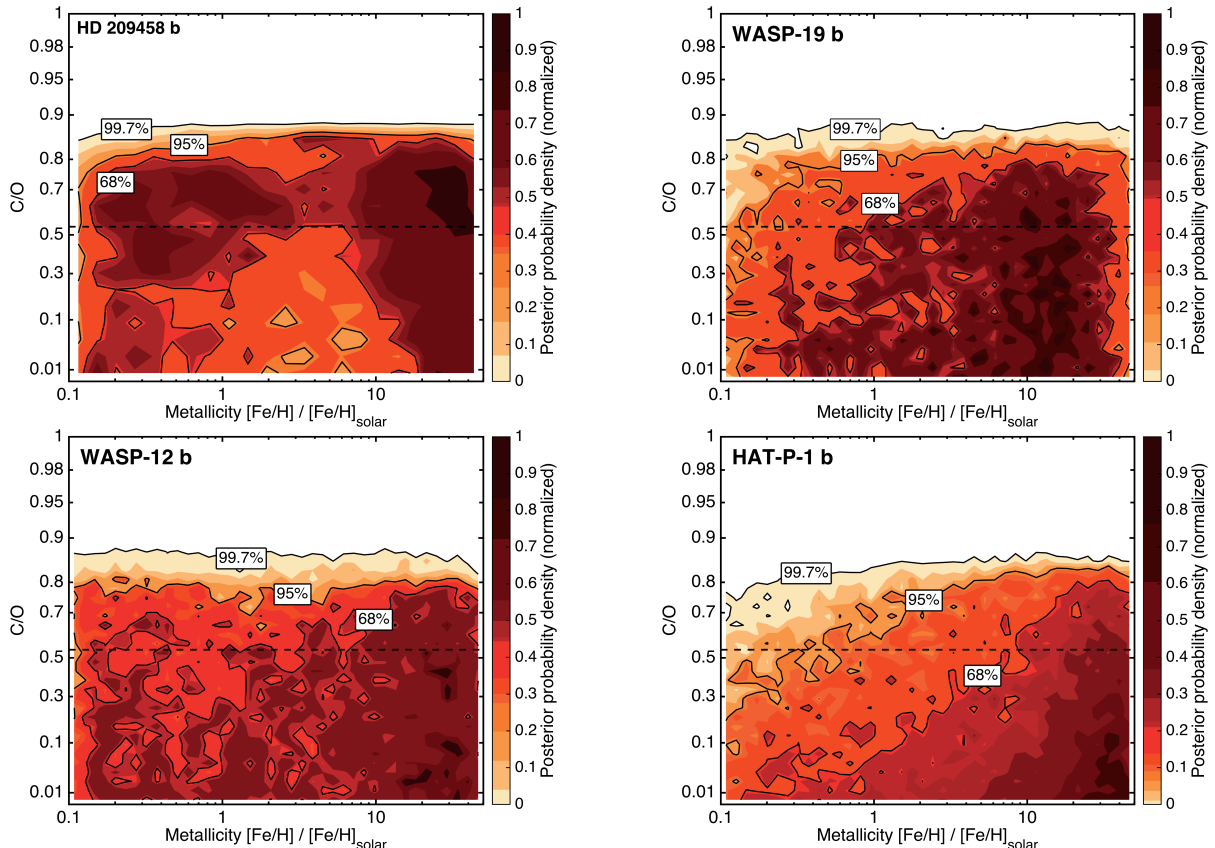


FIG. 5.— Joint constraints on the metallicity and C/O ratio in the deep atmospheres of HD 209458b, WASP 19b, WASP-12b, and HAT-P-1b. The coloring indicates the normalized posterior probability marginalized over all remaining atmosphere and cloud parameters. Black contours mark the 68% (1σ), 95% (2σ), and 99.7% (3σ) Bayesian credible regions. The *HST WFC3* transmission spectra of all four planets reveal robustly oxygen-dominated ($C/O < 0.9$) atmospheres. Constraints on the metallicity, i.e. the overall fraction of species heavier than He relative to solar, are weak. Results are shown for a cloud model in which the particle size and vertical cloud density profile are described by free parameters in the fit (Section 3.3.3). The posterior distribution is marginalized over the cloud parameters, the eddy diffusion coefficient, the planetary Bond albedo, the dayside-night side heat redistribution.

pling algorithm are described in Skilling 2004; Feroz et al. 2009; Benneke & Seager 2013 and its first application to atmospheric retrieval is discussed in Benneke & Seager (2013). Here, I provide overview of the technique and its unique capabilities specifically for atmospheric retrieval.

Similar to the widely used Markov Chain Monte Carlo (MCMC), nested sampling is a Monte Carlo approach to efficiently compute the multidimensional posterior distribution of model parameters in parameter estimation problems. The main advantage of nested sampling for atmospheric retrieval is, however, that nested sampling reliably captures highly non-Gaussian and multimodal posterior distributions (e.g. Feroz et al. 2009; Benneke & Seager 2013). This is extremely important for atmospheric retrieval because strong correlations and degeneracies between atmospheric parameters are common due to the generally sparse data available for exoplanets and the complex way in which vital information about planet is encoded in the observable planetary spectrum. Importantly, nested sampling also provides an excellent overview of the goodness-of-fit all across the entire parameter space, even in regions far away from the maximum probability (e.g., Figure 8). This provides an improved ability to assess which regions of the parameters space can be excluded at levels of significance higher than the commonly stated 95% or 99.7% probability.

Nested sampling begins by randomly taking a user-

specified number of “active samples” ($N \approx 100 \dots 10000$) from the *entire* prior parameter space. The active samples are then migrated towards regions of high likelihood by repeatedly replacing the lowest-likelihood sample by a new sample with a likelihood higher than the sample to be rep. In this “outside-in” approach, the complete prior parameter space is traversed providing high confidence that the global minimum is identified and that extremely correlated or banana-shaped posteriors are captured correctly. Replaced samples are stored such that a relatively good description of the probability across the entire parameters space can be inferred. In this work, I employ simultaneous ellipsoidal nested sampling to efficiently find sample with likelihoods higher than the previously lowest-likelihood sample (Feroz et al. 2009).

4. RESULTS

In this section, I present constraints on the atmospheric composition and cloud properties in eight hot Jupiters (HD 209458b, WASP-19b, HAT-P-1b, and XO-1b, HD 189733b, WASP-12b, WASP-17b, and WASP-43b) based on their measured transmission spectra. To capture the uncertainty in the atmosphere composition introduced by the broad variety of plausible cloud properties, I present constraints on the composition based on the “parameterized particle size and cloud profile” model. Cloud-introduced uncertainties on the composition are

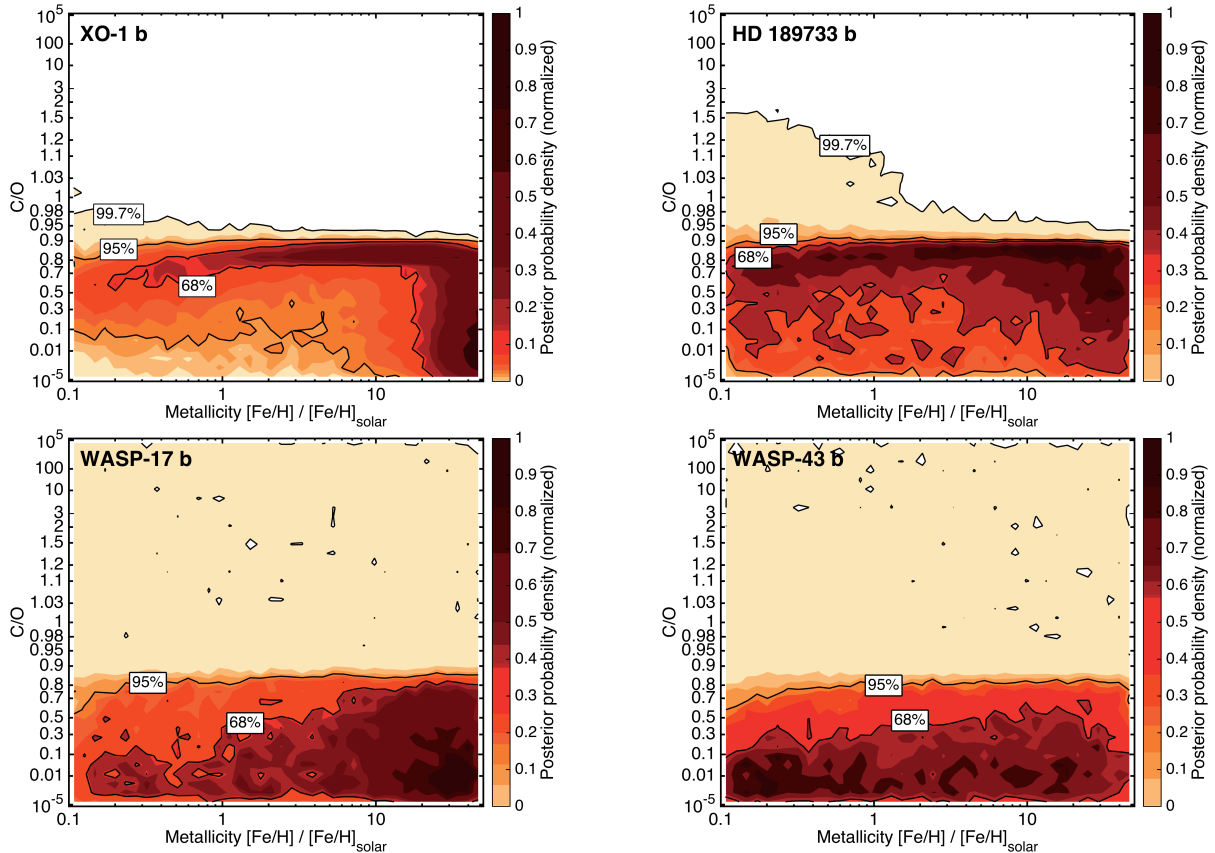


FIG. 6.— Same as Figure 5, but for the hot Jupiters XO-1b, HD 189733b, WASP-17b, and WASP-43b. The *HST WFC3* transmission spectra of all four planets favor $C/O < 0.9$ atmosphere at greater 95% confidence. A low-probability tail towards high C/O remains for WASP-17b, and WASP-43b containing a few percent of the posterior probability. To illustrate the tail, the probability is plotted over the full range from $C/O = 10^{-5}$ to $C/O = 10^{+5}$. (Madhusudhan et al. 2011; Stevenson et al. 2014).

TABLE 2
SUMMARY OF PLANET AND STELLAR TEMPERATURES, GOODNESS-OF-FIT, AND C/O CONSTRAINTS.

Planet	HD 209458b	WASP-19b	WASP-12b	HAT-P-1b	XO-1b	HD 189733b	WASP-17b	WASP-43b
T_{Eq} [K] for $A_B = 1$	1409	2013	2517	1271	1176	1169	1508	1340
$T_{*,\text{eff}}$ [K]	6065	5500	6300	5975	5750	5040	6550	4400
χ^2_{min}	30.8	1.4	4.0	26.8	35.5	17.5	14.4	24.8
χ^2_{min}/N	1.07	0.37	0.58	0.98	1.13	0.81	0.89	1.09
C/O (95% limit)	< 0.86	< 0.82	< 0.80	< 0.77	< 0.87	< 0.92	< 0.89	< 0.87
C/O (99.7% limit)	< 0.88	< 0.85	< 0.87	< 0.84	< 0.98	< 1.20	—	—
$(\Delta\chi^2)_{\text{min}}$ for $C/O > 1$	55.9	13.3	36.0	22.9	12.6	7.1	10.0	6.9
$\mathcal{L}_{\text{max}}/\mathcal{L}_{C/O > 1}$	$1.4 \cdot 10^{12} : 1$	788 : 1	$7.0 \cdot 10^7 : 1$	99,720 : 1	553 : 1	35 : 1	153 : 1	32 : 1

fully accounted for by marginalizing over the wide range of cloud parameters in this model (Section 4.1-4.2). The compositional constraints presented in this section solely rely on the *HST WFC3* observations, and do not depend on comparisons of observations taken at different times and different instruments. In Section 4.4, I then present constraints on the cloud properties using both the “parameterized particle size and cloud profile model” as well as a simplified “gray cloud deck + Rayleigh haze model”. *HST STIS* and *Spitzer* observations are included to supplement to conclusions on cloud properties.

4.1. C/O and Metallicity

The main result of this study is that all eight hot Jupiters with detectable near-infrared absorption features show a strict upper limit on the C/O ratio at approximate 0.9. Carbon-rich atmospheric compositions

($C/O > 1$) are firmly ruled out for HD 209458b, WASP-19b, WASP-12b, HAT-P-1b, and XO-1b — virtually no posterior probability exists for atmospheric compositions with $C/O > 0.9$ (Figure 5). The remaining two hot Jupiters (HD 189733b, WASP-17b, and WASP-43b) show similar posterior distributions; however, a low-probability tail (<5% probability) remains towards high C/O given currently available data (Figure 5). Meanwhile, the available observations provide virtually no constraint on the atmospheric metallicity for any of the planets.

The upper limit of $C/O < 0.9$ is a robust finding. The nested sampling algorithm explores every corner of the multi-dimensional parameter space, ranging from $C/O < 10^{-5}$ (10^5 times more oxygen) to $C/O < 10^5$ (10^5 times more carbon), and there is no atmospheric scenario

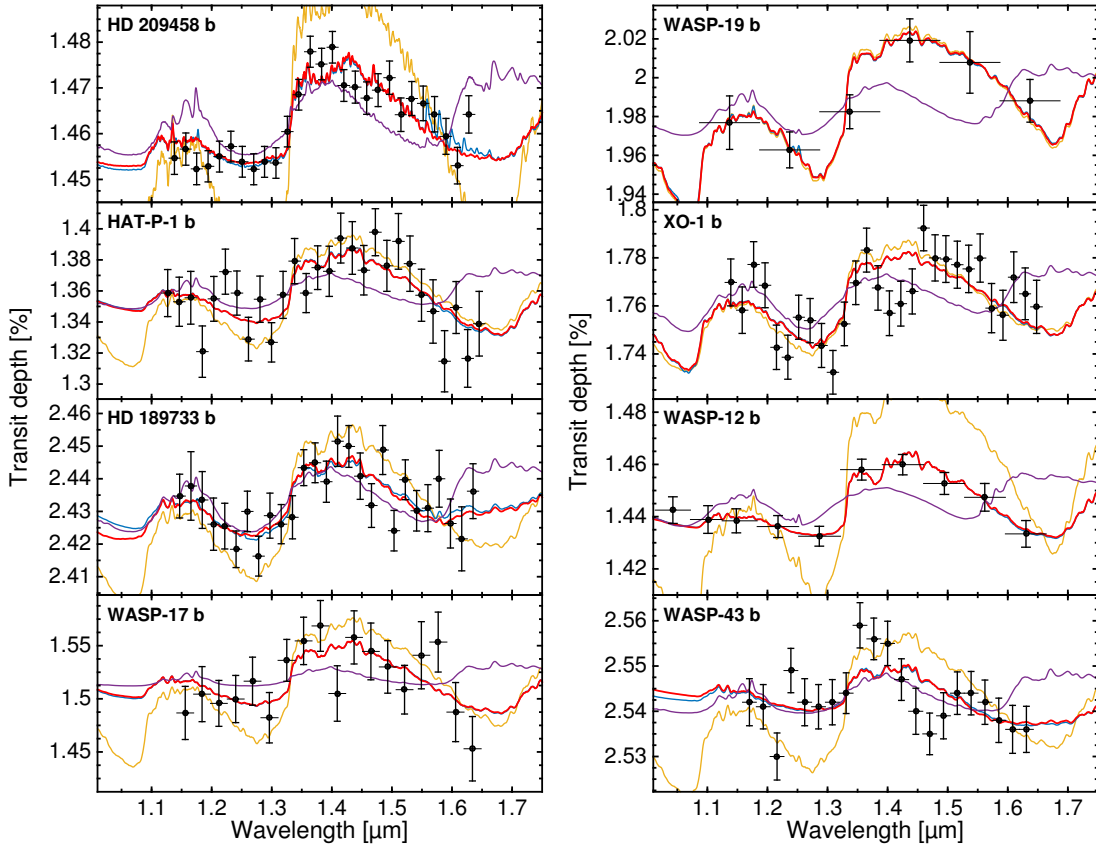


FIG. 7.— Model transmission spectra compared to the published *HST WFC3* transit depth measurements (black). Solid lines show the transmission spectra for a fiducial clear solar composition atmosphere (yellow), the overall best-fitting model (red), the best-fitting solar composition atmosphere with clouds (blue), and the best fitting $C/O > 1$ model with clouds (purple). Plotted observations and their $1 - \sigma$ uncertainties are taken from Deming et al. (2013) for HD 209458b and XO-1b, Huitson et al. (2013) for WASP-19b, Wakeford et al. (2013) for HAT-P-1b, McCullough et al. (2014) for HD 189733b, Kreidberg et al. (2015) for WASP-12b, Mandell et al. (2013) for WASP-17b, and Kreidberg et al. (2014b) for WASP-43b. The model spectra have a vast number of molecular lines; for clarity the spectrum has been Gaussian smoothed.

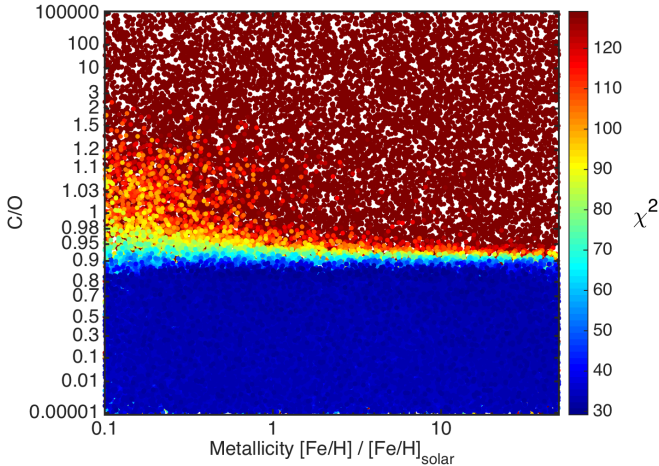


FIG. 8.— χ^2 of all atmospheric models in the nested sampling results for HD 209458b. The upper limit $C/O \lesssim 0.9$ is extremely robust. The nested sampling algorithm explored all corners of the multi-dimensional parameter space, ranging from $C/O < 10^{-5}$ (100,000x more oxygen) to $C/O < 10^5$ (100,000 times more carbon). All atmospheric scenario with $C/O > 1$ are excluded at $\Delta\chi^2 > 55.9$, corresponding to a likelihood ratio of $1.4 \cdot 10^{12}$ to 1. The fit to the data is excellent ($\chi^2/N = 1.1$) $C/O \lesssim 0.9$ and drops off sharply near $C/O = 0.9$ to $\chi^2/N \gtrsim 4$.

with $C/O > 0.9$ that results in a good fit to the data. As an example, the fit to the data degrades sharply from $\chi^2/N = 1.1$ to worse than $\chi^2/N = 4$ for C to O ratios

above 0.9. (Figure 8).

The chemical explanation for the strict upper limit on the C/O ratio is that the observed water absorption feature at $1.4 \mu\text{m}$ can only exist if substantially more oxygen is present in the gas envelope than carbon (Figure 7). As the C/O ratio approaches unity, almost all of the oxygen becomes trapped in CO molecules leaving no oxygen left to form H_2O . The upper limit on the C/O ratio is largely independent of the metallicity because the atmospheric chemistry at the high temperatures encountered in hot Jupiters sharply changes between $C/O = 0.8$ and $C/O = 1$.

Methane and water have strongly overlapping absorption bands in the WFC3 bandpass at 1.15 and $1.4 \mu\text{m}$ (Figure 9). Nonetheless, I can unambiguously distinguish between H_2O absorption (oxygen-dominated chemistry) and CH_4 absorption (carbon-dominated chemistry) because the relative strengths of the 1.15 and $1.4 \mu\text{m}$ absorption features are vastly different for water and methane. Methane absorption bands at 1.15 and $1.4 \mu\text{m}$ are similarly strong and would inevitably result in two similarly strong absorption features at 1.15 and $1.4 \mu\text{m}$, which is not in agreement with the data.

Finding a lower limit on the C to O ratio is not possible because no carbon-bearing species can be inferred from the data and a wide range of water abundances is consistent with the detected water absorption feature

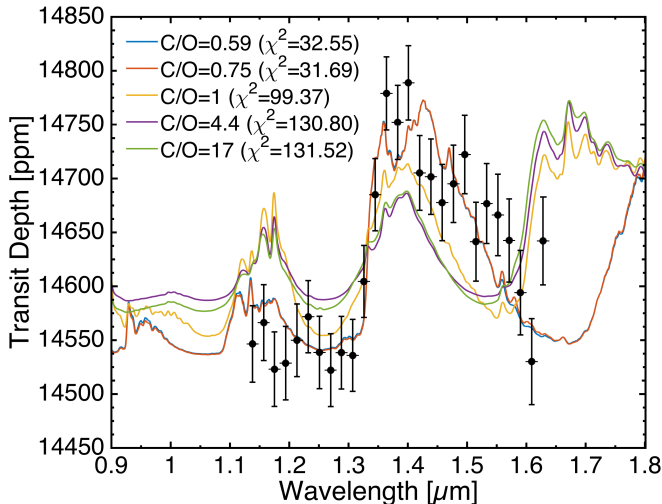


FIG. 9.— Effect of the C/O ratio on the *WFC3* transmission spectrum of HD 209458b. Colored curves show the best-fitting model spectra at $C/O=0.59$ (blue), $C/O=0.75$ (red), $C/O=1$ (yellow), $C/O=4$ (purple), and $C/O=17$ (green). Best-fitting model are obtained by fixing the C/O ratio and optimizing all other model parameters including the cloud properties. Water and methane have strongly overlapping absorption bands in the *WFC3* bandpass (Benneke & Seager 2013); the increased transit depth at 1.15 and 1.4 μm is due H_2O absorption for $C/O < 1$ (oxygen-dominated chemistry), but due to CH_4 absorption for $C/O > 1$ (carbon-dominated chemistry). All best-fitting models contain a thick cloud deck between 2 and 17 mbar to match the relative small amplitude of the observed absorption features. $C/O < 1$ is in good agreement with the observations — clouds in the 1-10 mbar regime mute the weaker 1.15 μm H_2O absorption features, while preserving the stronger 1.4 μm feature. $C/O > 1$ is in strong disagreement with the data; however, because the methane absorption bands at 1.15 and 1.4 μm are similarly strong and would inevitably result in two similarly strong absorption features at 1.15 and 1.4 μm , which is not observed.

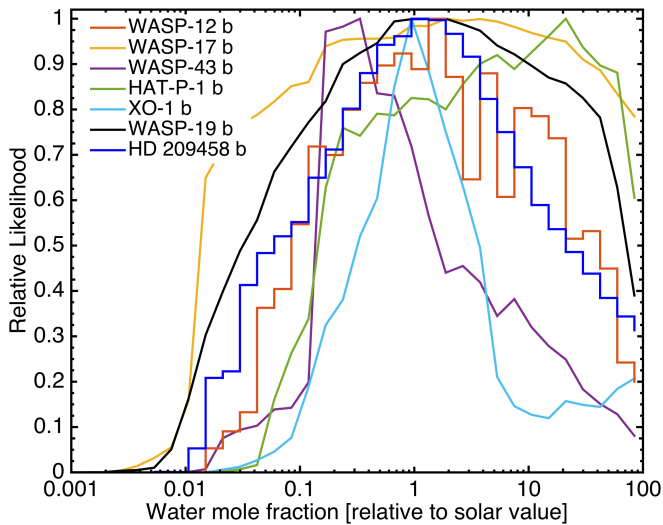


FIG. 10.— Constraints on the water mole fraction for eight hot Jupiters. Colored curves indicate the relative likelihood of the water mole fraction at 100 mbar relative to the value expected for solar composition atmospheres (~ 610 ppm). The water abundances of all eight planets are in agreement with solar composition. A relatively wide range of water abundances is in agreement with the observations due to strong correlation between the water mole fraction and the cloud top pressure (see also Figure 12). Accounting for clouds in the atmospheric retrieval model, I do not confirm the inference of sub-solar water abundances for HD 209458b and HD 189733b (Madhusudhan et al. 2014b).

(Fig. 10). The detection of a single absorption feature in low-resolution transmission spectroscopy generally provides weak constraints on the abundance of that absorber (Benneke & Seager 2012). The shape and depths of the absorption features are predominately determined by the scale height and cloud properties, and are only indirectly dependent of the absorber abundance.

4.2. Water Abundance

The water abundances of all eight hot Jupiters are consistent with the value expected for solar composition (Figures 10). Although previous studies (Madhusudhan et al. 2014b) have reported low water abundances and/or high carbon-to-oxygen ratios on HD 209458b, HD 189733b, and WASP-12b, we find that these conclusions are not supported by the data once the full range of clouds is considered in the retrieval modeling. It is worth noting that the uncertainty in the water abundance is predominately driven by the strong correlation between water abundance and cloud top pressure (Figures 10). The relatively small depths of the water absorption features at 1.4 μm as compared to cloud free scenarios clear can equally well be explained by scenarios with low water abundance and low-altitude clouds (240 mbar) or by solar water abundance scenarios with clouds between 1 and 100 mbar (Figure 12). The correlation between cloud top pressure and water abundance explain why lack of clouds in the retrieval modeling would lead to the conclusion of low water abundance as discussed in the following section.

4.3. Importance of Considering A Wide Range of Clouds

The constraints on the atmospheric composition depend sensitively on the range of clouds and hazes considered in the retrieval model. It is therefore important to account for all plausible cloud scenarios when retrieving the atmospheric composition. As an example, Figure 11 compares the C to O ratio constraints for HD 209458b for three different clouds models. Without the presence of clouds, the only explanation for the relative shallow water absorption feature in the *WFC3* observations of HD 209458b (Fig. 7) is a sub-solar water abundance and high C/O ratio (Figure 11 left). The presence of clouds, however, presents an alternative explanation for the observed shallow absorption feature, resulting in much weaker constraints on C/O (Figure 11 center and right). The sensitivity of the atmospheric composition constraints is a result of strong degeneracies between the atmospheric composition and cloud properties in low resolution transmission spectra (Figure 12).

4.4. Cloud and Haze Properties

The observed transmission spectra indicate the presence of optically thick cloud decks in the mid-atmospheres of HD 209458b and WASP-12b (Section 4.4.1). The clouds decks are found consistently using both the “cloud deck + Rayleigh haze” model as well as the “parameterized cloud profile and particle size” model. HD 189733b may host a similar gray cloud deck if star spots affect the spectrum (Section 4.4.2); otherwise thin haze are required as previously suggested. No clouds or hazes are inferred for WASP-19b, XO-1b, WASP-17b, and WASP-43b.

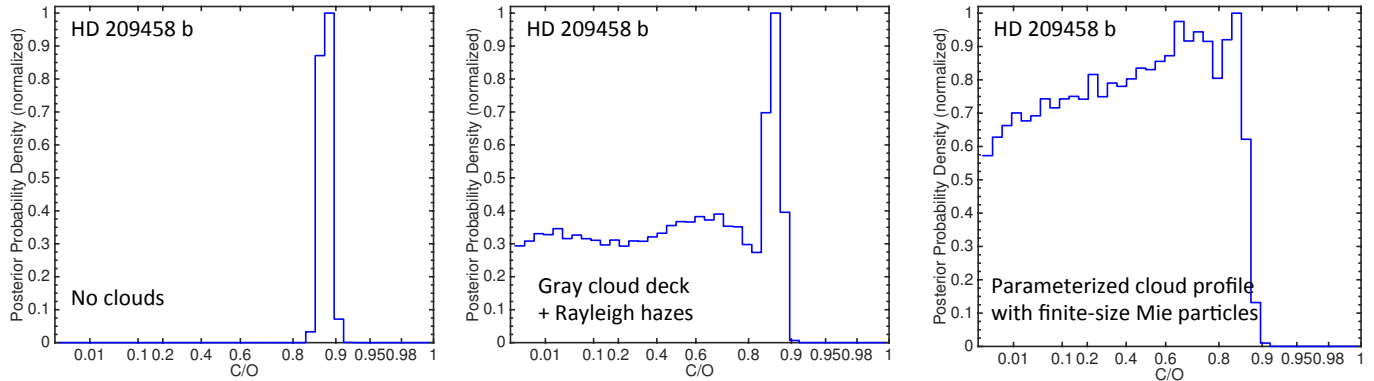


FIG. 11.— The constraints on the C/O ratio depend sensitively on the range of clouds considered in the retrieval modeling. The three panels illustrate the posterior probability density as function of C/O ratio for HD 209458b assuming no clouds (left), accounting for a gray cloud deck and Rayleigh hazes (center), and accounting for wide range of clouds using a parameterized cloud profile and particle size distribution (right). The plotted posterior probability distributions are marginalized over the model parameters listed in Table 2. Completely ignoring the potential presence of clouds leads one to the conclusion of high C/O ratio ($C/O = 0.88 \pm 0.04$) and low water abundance (left). The peak for the retrieval model without clouds (left) is narrow because only atmospheres with a narrow range of water abundances corresponding to $C/O \approx 0.88$ fit the relatively small water feature in the absence of clouds. However, only an upper limit at $C/O=0.89$ can be inferred when clouds are considered in the modeling. For the gray cloud deck + Rayleigh hazes model (center), a peak at $C/O=0.89$ remain, but a long probability tail towards $C/O \rightarrow 0$ exists (center). No lower bound on C/O available. The peak at $C/O \approx 0.88$ also disappears in the parameterized cloud profile and particle size model (right). The C/O results presented in this work use this parameterized cloud profile and particle size model (right) to fully account for the wide range of plausible clouds on hot Jupiters.

4.4.1. Cloud Decks on HD 209458b, WASP-12 b, and WASP-31b

It is instructive to investigate the constraints on cloud top pressure and haze opacity from the simple “gray cloud deck + Rayleigh hazes” model. This two-parameter cloud model simultaneously allows for a gray cloud deck at a parameterized cloud top pressure as well as “Rayleigh” hazes with parameterized opacity composed of small particles ($r_p \ll \lambda$). Within this model, the *HST WFC3* observations of HD 209458b and WASP-12b strongly indicate the presence of a thick cloud deck. All scenarios without clouds are ruled out at greater 99.7% confidence (Figures 12). Based on the depth of the observed water feature size, I infer that the upper cloud deck is in the mid-atmosphere between approximately 200 mbar and 0.01 mbar for HD 209458b and 30 mbar and 0.01 mbar for WASP-12b. Stronger constraints on the cloud top pressure are not available because the cloud top pressure is strongly correlated with the water mole fraction (Figure 12). For HD 209458b, equally good fits to the data are obtained for a wide range of atmospheric scenarios ranging from low water abundances (1% solar) and low-altitude clouds (200 mbar) to high water abundances (10 x solar) and high-altitude clouds (0.01 mbar). The clouds in the atmosphere of WASP-12b are between 0.01 mbar for 5% solar water abundance and 10 mbar for 10 times the solar water abundance (Figure 12). The inferred clouds top pressure for a given water mole fraction is lower for WASP-12 b because the observed water absorption feature is weaker as compared to the cloud free model transmission spectrum than for HD 209458b (Figure 7). The presence of clouds can be inferred from the WFC3 observations alone, but is also strongly supported by the *HST STIS* observations (Figure 15).

The negative correlations between water mole fraction and cloud top pressures in Figure 12 can be explained as follows. High clouds reduce the depths of near-IR water absorption features. In contrast, increasing the water abundance strengthens the water absorption features for

a given cloud top pressure. Different combinations of water mole fraction and cloud top pressure, therefore, result in the same depths of the $1.4 \mu\text{m}$ water absorption feature and similar good fits to the data.

Modeling the cloud particles using Mie scattering reveals that particles with effective diameters above $1 \mu\text{m}$ are most probable (Figure 14). Large particles naturally explain the gray nature of the observed cloud signature. Both the 1.15 and $1.4 \mu\text{m}$ water absorption features are diminished, as expected for a sharp, wavelength-independent cutoff of the grazing star light below the cloud top pressure. It is interesting to note, however, that small particles can similarly appear gray in exoplanet transmission spectra despite their non-gray scattering properties, if the particle density increases sharply near the cloud top. A sudden rise in particle number density at a given altitude can lead to the cutoff of all grazing light beams below that altitude, largely independent of the wavelength. The effect of cloud particles on exoplanet transmission spectra depends not only on the scattering properties of the particles, but also sensitively on the vertical distribution of the particles in the atmosphere.

One caveat for HD 209458 b is that the $1 \mu\text{m}$ data point at the red end of the HD209458b *HST STIS* observations cannot be fit by any model spectrum. Water, TiO, and VO are plausible absorbers at $1 \mu\text{m}$, but cannot account for the increased transit depth without also increasing the transit depth in the surrounding *HST STIS* and *WFC3* transit depth measurements. The increased transit depth measurement may either be caused by an unknown opacity source or systematic effects potentially related to the fringing of the STIS CCD may have affected the measurement.

Similarly, the *Spitzer* measurement at 3.6 and $4.5 \mu\text{m}$ cannot be fit to better than $1.5 - \sigma$ when simultaneously fitting the *HST STIS*, *WFC3*, and *Spitzer* data points (Figure 15b). While the $1.5 - \sigma$ deviation of two points does not substantially degrade the overall statistical fit to the data; it is worth a discussion because they are the

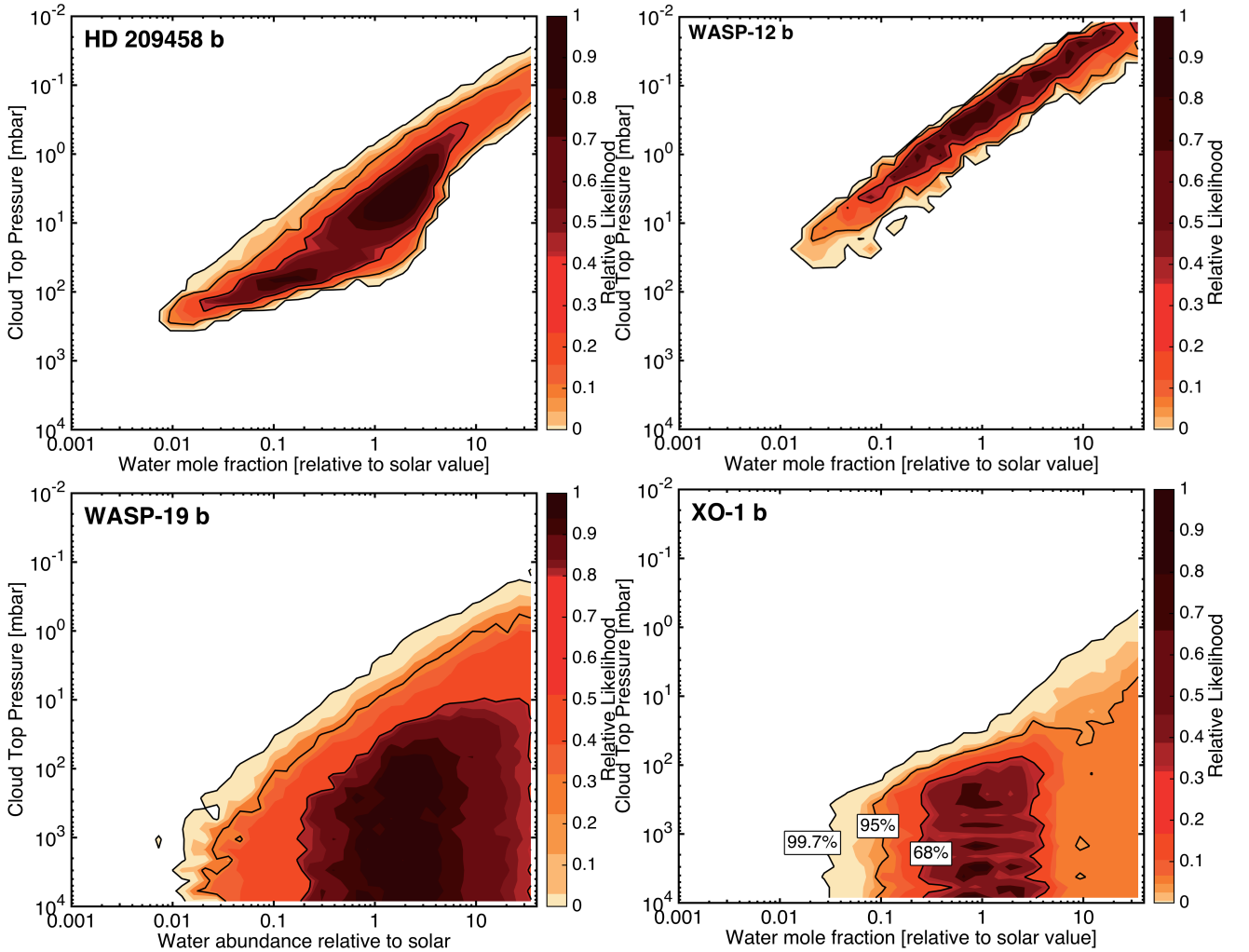


FIG. 12.— Joint constraints on the water abundance and cloud top pressure for HD 209458b, WASP-12b, WASP-19b, and XO-1b. The colored shading indicates the relative likelihood of atmospheric models as a function of water mole fraction and cloud top pressure. Black contours mark the 68% (1σ), 95% (2σ), and 99.7% (3σ) confidence regions, assuming a log-uniform prior on the water mole fraction. Scenarios with largely cloud-free atmosphere are near the bottom of each panel; scenarios with high altitude clouds are at the top. Clouds are required on HD209458b and WASP-12b at greater than 99.7% confidence. Water abundance and cloud top pressure are highly correlated, preventing precise constraints on water abundance and cloud top pressure individually. For WASP-19b and XO-1b, current observations do not distinguish between cloud free scenarios and scenarios with low-altitude clouds. Scenarios with and without clouds are in agreement with the data. The lower limit on the cloud top pressure depends on the water abundance.

only measurements red of $3\ \mu\text{m}$. Sing et al. (2013) and Stevenson et al. (2014) suggested that the entire UV to near-IR spectrum is sloped due to small particle hazes. However, the new *HST WFC3* data by Kreidberg et al. (2015) rule out this scenario unless they are substantially offset to the *HST STIS* data. No plausible model exists that would simultaneously fit the reported *HST STIS*, *WFC3*, and *Spitzer* data points to within better than $1.5 - \sigma$. If water absorption increases the transit depth to 1.46% at $1.4\ \mu\text{m}$, then the absorption of the same water vapor would result in a transit depth between 1.44% and 1.5% in the *Spitzer* bandpasses, independent of the cloud or haze properties. Possible explanation are that the transit depth measurements are low due to random chance or that they are affected by star spots (McCullough et al. 2014), WASP-12 b’s stellar companion (Stevenson et al. 2014), stellar variability, or uncorrected instrumental effects.

WASP-17b and WASP-43b show water absorption features weaker than expected for a cloud free solar com-

position atmosphere (Figure 7), which may indicate the presence of clouds similar to HD 209458b. However, the data is insufficient to rule out low water abundance scenarios without clouds for WASP-17b and WASP-43b.

The observations of WASP-19b and XO-1b do currently not indicate the presence of clouds or hazes. Instead, the observations provide a strict lower limit on the opacity of small-particle “Rayleigh” hazes in the upper atmosphere. For WASP-19b, no cloud deck exists above the 10 mbar level for solar water abundance and 0.1 mbar for 50 x solar (Figure 12). Similar, if small particle hazes are present, their opacity does not exceed $\sigma_{R,400} = 10^{-4}\ \text{m}^2/\text{kg}$ for a solar metallicity atmospheres and $\sigma_{R,400} = 1\ \text{m}^2/\text{kg}$ for a 50 x solar metallicity atmospheres. Higher values for haze opacity would mute the H_2O absorption features in the *HST WFC3* bandpass and result in a sloped visible and NIR transmission spectrum, which is not in agreement with the observations. Qualitatively the results are similar for XO-1b (Figure

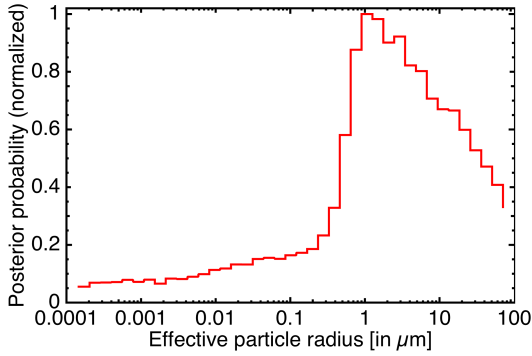


FIG. 13.— Observational constraints on effective particle size of the clouds on HD 209458b. The most probably scenarios for the clouds on HD 209458b are large particles ($>1 \mu\text{m}$). Smaller particles cannot fully be ruled out, however, because a sharp upper cloud deck would mask the strongly wavelength-dependent scattering properties of small particles in transmission spectra (see also Figure 14). The assumed particles are Mie scattering particles with the complex refractive indices of MgSiO_3 .

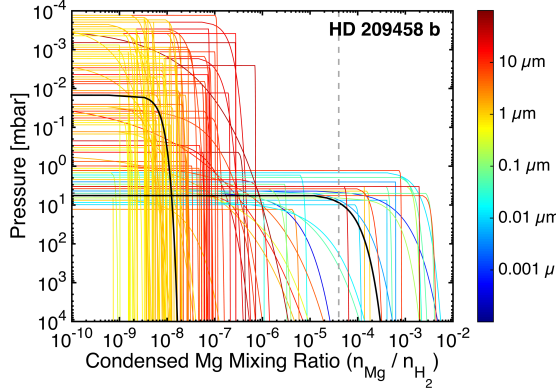


FIG. 14.— Observational constraints on the vertical cloud density profiles for MgSiO_3 grains in the atmospheres of HD 209458b and HAT-P-1b. Representative cloud density profiles are plotted for scenarios that are within a likelihood ratio of 300:1 ($\Delta\chi^2 < 11.8$) of the best fit to the observations. For illustrative purposes, cloud profiles are shown for near solar composition atmospheres only ($0.5 < M < 5$; $0.3 < C/O < 0.6$). The cloud density is represented by the ratio between the number of condensed MgSiO_3 molecules and the number of background H_2 molecules. The solar abundance number ratio $\text{Mg}/\text{H} = 4 \cdot 10^{-5}$ is indicated as a vertical dashed line. Colors indicate the effective particle radii for each of the cloud profiles. Two distinct types of clouds scenarios are in agreement with the observations of HD 209458b: 1) a sharp cloud deck near 1-10 mbar with a cloud free upper atmospheres or 2) thin clouds composed of large particles ($>1 \mu\text{m}$) reaching to high altitudes. Both scenarios reduce the amplitude of NIR molecular feature in a largely wavelength-independent way. In contrast, HAT-P-1b must host thin, small-particle ($\lesssim 0.1 \mu\text{m}$) reaching to high altitude ($>1 \text{mbar}$) to explain the enhanced opacity at visible wavelength.

12).

4.4.2. HD 189733b: Small-Particle Hazes or Gray Cloud Deck?

The reported transmission spectrum of HD 189733b shows a prominent slope at short-wavelength with increasing transit depth from the near-IR ($1 \mu\text{m}$) to the ultraviolet (300 nm) (Figure 15a). This slope has traditionally been attributed to scattering of non-absorbing, Rayleigh scattering dust (Lecavelier des Etangs et al. 2008; Sing et al. 2011; Pont et al. 2013). Recently, McCullough et al. (2014) suggested that unocculted star spots may be responsible for the apparent slope in the transit depth, reinterpreting the spectrum of

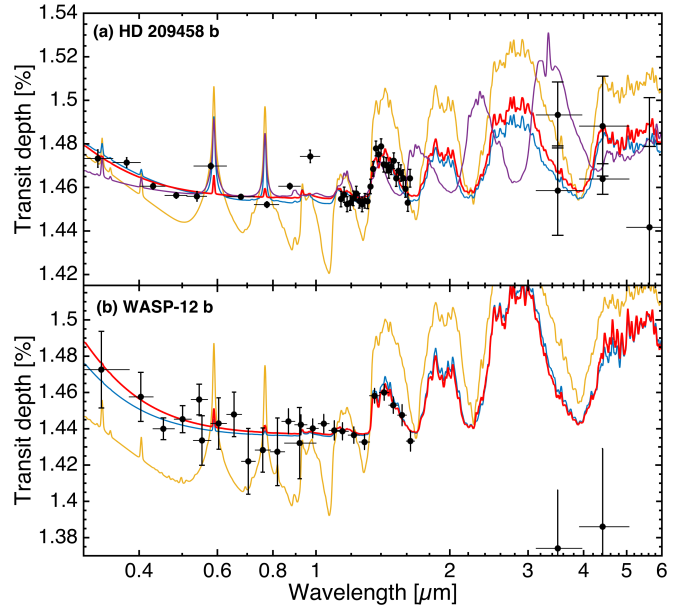


FIG. 15.— Ultraviolet to near-infrared transit depth measurements of HD 209458b and WASP-12b compared to model transmission spectra. Solid lines show the transmission spectra for a fiducial clear solar composition atmosphere (yellow), the overall best-fitting model (red), the best-fitting solar composition atmosphere with clouds (blue). Black circles indicate the transit depth measurement and their $1-\sigma$ uncertainties taken from Knutson et al. (2007), Deming et al. (2013), Evans et al. (2015), and Crossfield et al. (2012b) for HD 209458b, and Sing et al. (2013) and Kreidberg et al. (2015) for WASP-12b. The observed transmission spectra indicate the presence of optically thick cloud decks on all three planets in the mid-atmospheres of HD 209458b and WASP-12b. Only the strong $1.4 \mu\text{m}$ water band, the cores of alkali lines, and the Rayleigh scattering signature blue of 500 nm are detectable.

HD 189733b’s with a cloud free atmosphere. In this section, I revisit the observed spectrum by (1) assuming that the reported measurements of the planet-to-star radius ratios are not affected by star spots, and (2) accounting for the presence of unocculted star spots. In the presence of star spots, I find that HD 189733b may have a cloud deck in the mid-atmosphere similar to HD 209458b, albeit at higher pressure. If confirmed, the cloud properties of HD 189733b and HD 209458b could be more similar than previously believed.

First, assuming that the reported measurements are not affected by star spots, I find that small-particle “Rayleigh” hazes significantly exceeding the opacity of molecular Rayleigh scattering must be present in the upper atmosphere of HD 189733b, in agreement with previous studies. Assuming a Rayleigh-like haze opacity ($\sigma \propto \lambda^{-4}$), the reference opacity at 400 nm, $\sigma_{R,400}$, is between $\sim 10^{-2} \text{m}^2\text{kg}^{-1}$ for low metallicity atmospheres and $\sim 10 \text{m}^2\text{kg}^{-1}$ for 50 x solar composition atmospheres. The inferred haze opacity exceeds the expected opacity by molecular Rayleigh scattering by a factor of 10 to 10,000. A strong correlation between haze opacity and atmospheric metallicity arises because different combinations of haze opacity and atmospheric metallicity result in identical relative transit depths between the visible and infrared spectrum. Increased metallicity increases transit depth in the near-IR, but the same relative transit depth between near-IR and visible wavelengths can be recovered if the haze opacity is increased simultaneously (Benneke & Seager 2012).

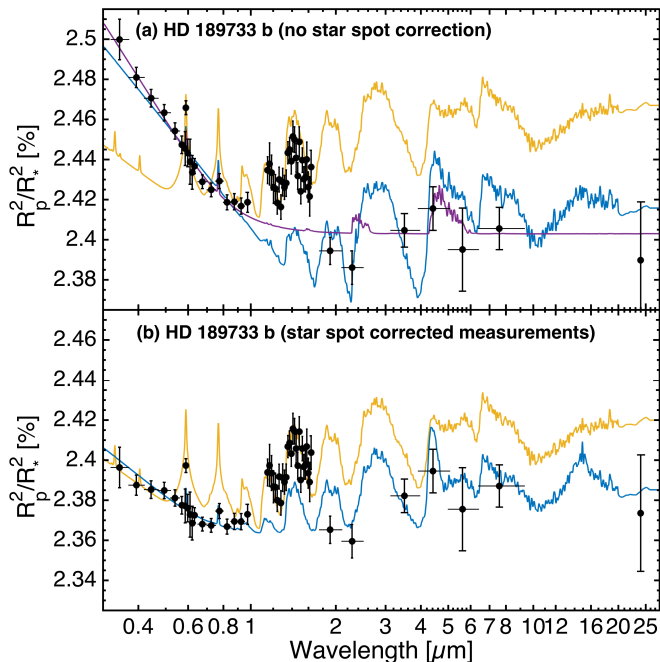


FIG. 16.— Ultraviolet to near-infrared transit depth measurements of HD 189733b compared to model transmission spectra. Black circles in panel (a) indicate the transit depth measurements directly as reported by Pont et al. (2013) and McCullough et al. (2014). Panel (b) shows $(R_p/R_*)^2$ based on the same measurements, but corrected for the presence of star spots according to McCullough et al. (2014) and assuming the best fitting star spot fraction and spot temperature. The star spot corrected measurements reveal that the spectroscopic appearance of HD 189733b can be similar to the one of HD 209458b and WASP-12b (Figure 15). Solid lines show the transmission spectra for a fiducial clear solar composition atmosphere (yellow), the best-fitting solar composition atmosphere with clouds and hazes (blue), and a theoretical model with only a cloud deck and high altitude hazes (purple). The originally reported transit depth measurements (panel a) strongly indicate the presence of high altitude, small-particle hazes to match the Rayleigh slope between 0.3 and 1. However, a significant offset of the *WFC3* data is required to match the data. After star spot correction (panel b), the measurements do not favor hazy atmospheric scenario, but are in better agreement with either a completely cloud free atmosphere with Na and K removed or scenarios with a thick cloud deck at 1-100 mbar similar to HD 209458b. Cloud-free scenarios without Na and K simultaneously match the *HST STIS* and *WFC3* with all *Spitzer* significantly offset. Cloudy scenarios matches the *Spitzer* and *HST STIS* observations with the *WFC3* offset. Plausible explanations for the suggested offsets are variability in unocculted star spot which would give additional support to the star spot hypothesis as an explanation for the short wavelength slope.

Alternatively, assuming that star spots affect the measured transmission, I correct the apparent transit depth measurement using the relation

$$\left(\frac{R_p}{R_*}\right)^2 = D \cdot \left[1 - \delta \left(1 - \frac{e^{hf/kT_{phot}} - 1}{e^{hf/kT_{spot}} - 1}\right)\right], \quad (7)$$

where D is the measured transit depth, R_p/R_* is the geometric planet-to-star radius ratio, δ is the star spot fraction, T_{spot} is the star spot temperature, T_{phot} is the effective temperature of the star’s photosphere, and $f = c/\lambda$ is the observing frequency (McCullough et al. 2014). The corrected transit depth, $(R_p/R_*)^2$, is illustrated in Figure 16(b) assuming the best fitting spot fraction $\delta = 4.6\%$ and spot temperature $T_{spot} = 4400\text{ K}$. After spot correction, the transmission spectrum of HD 189733b shows similar trends to HD 209458b

and WASP-12b. Similar to HD 209458b and WASP-12b, a gray cloud deck may be present on HD 189733b that reduces the depth of the water absorption feature at $1.4\ \mu\text{m}$ and mute the wide wings of potassium and sodium. Molecular Rayleigh scattering in the high atmosphere is visible at wavelength shorter than $500\ \text{nm}$.

5. SUMMARY & CONCLUSIONS

I have introduced a novel approach to interpret spectroscopic observations of planetary atmospheres that combines the statistical robustness and exploratory nature of atmospheric retrieval methods (Rodgers 2000; Madhusudhan & Seager 2009; Benneke & Seager 2012; Line et al. 2013b) with the self-consistency and ability to provide physical insights of complex atmospheric forward models (Burrows et al. 1997, 2005; Marley et al. 2002; Fortney et al. 2008, 2011; Moses et al. 2011b). Rather than retrieving only molecular abundances as free parameters, the new “SCARLET” approach can provide direct insights into the elemental composition of the deep atmosphere based on observations of the upper atmosphere.

In this work, I applied the new SCARLET framework to eight transiting hot Jupiters with detected molecular absorption features in their near-infrared transmission spectra (HD 209458b, WASP-19b, HAT-P-1b, XO-1b, HD 189733b, WASP-12b, WASP-17b, and WASP-43b). My main findings are as follows:

1. The C/O ratios in the deep atmospheres of all eight hot Jupiters are consistently below 0.9. This result strongly indicates that gas envelopes of most hot Jupiter are not carbon-dominated ($C/O > 1$). The finding of $C/O \lesssim 0.9$ is robust for HD 209458b, WASP-19b, WASP-12b, HAT-P-1b and XO-1b (Table 2). A comprehensive exploration of the parameter space reveals that any scenario with $C/O > 1$ is excluded at high significance. All carbon-rich scenarios ($C/O > 1$) for HD 209458b, for example, are excluded at $\Delta\chi^2 > 55.9$ (likelihood ratio of $1.2 \cdot 10^{12}$ to 1). The finding of $C/O \lesssim 0.9$ relies solely on *HST WFC3* transmission spectroscopy, which has been shown to provide repeatable and reproducible measurements (e.g., Kreidberg et al. 2014a). No lower limit is provided because all C/O ratios smaller than 0.9 are equally plausible for all eight planets.
2. The water abundances for all eight planets are consistent with the value expected for a solar composition. For HD 209458b, I find that the relatively small depth of the $1.4\ \mu\text{m}$ water absorption feature as compared to a clear solar composition atmosphere is due to the presence of a cloud deck, not due to a low water abundance as suggested by Madhusudhan et al. (2014b). In general, the constraints on the water abundance remain weak and are driven by the strong correlations between the water abundance and cloud top pressure.
3. Current observations of transiting hot Jupiters provide no meaningful constraints on the overall abundance of metals in the atmospheres. All metallicity values in the probed range between 0.1 and 100 times solar metallicity are in good agreement with the observed transmission spectra. (Benneke & Seager 2012). HD 189733b may host a similar gray cloud deck if star spots affect the spectrum.

4. Clouds on hot Jupiters are common over a wide range of equilibrium temperatures. The transmission spectra of HD 209458b ($T_{\text{eq}} = 1400$ K) and WASP-12 b ($T_{\text{eq}} = 2500$ K) strongly indicate the presence of cloud decks in the mid-atmosphere. The cloud top pressure is between 0.01 mbar and 200 mbar at 99.7% confidence, strongly correlated with the atmospheric water abundance. HD 189733b may host a cloud deck similar to HD 209458b and WASP-12 b, rather than the suggested Rayleigh hazes, if star spots affect the observed spectrum.
5. An important lesson from this study is that the constraints on the atmospheric composition depend sensitively on the range of clouds and hazes considered in the retrieval model. Ignoring the presence of clouds or describing the clouds with a more restricted model may produce overly optimistic constraints on the atmospheric compositions. In this work, I account for a broad variety of cloud properties and derive reliable constraints on composition by marginalizing over free parameters describing the particle size and density profile of the clouds.
6. The posterior probability distributions of atmospheric parameters obtained from low signal-to-noise exoplanet spectra are highly non-Gaussian. Parameters, such as the C/O ratio, may have only one-sided constraints or long tails at low probability. In this regime, presenting the traditional $\pm 1-\sigma$ (68%) uncertainties can be extremely misleading because long tails reaching to values far from the reported best-fit may substantially change the interpretation of the results. In this work, I discuss 99.7% confidence limits whenever possible and provide likelihood ratios to assess our confidence in excluding atmospheric scenarios.

5.1. Implications for Planet Formation

The upper limit of 0.9 on the C/O ratio has important implications for the formation of hot Jupiters. Protoplanetary disk models suggest that oxygen near the disk’s mid-plane freezes out efficiently beyond the water ice-line, resulting in oxygen-depleted gas between water ice line and CO lines (Öberg et al. 2011). Helling et al. (2014) showed that the protoplanetary gas between water and CO ice lines should transition to $C/O \rightarrow 1$ on timescales of ~ 3 Myrs set by cosmic-ray induced unblocking of O_2 and CO. Assuming that most of the giant planet envelope directly accretes from this protoplanetary gas, the formation of giant planets with carbon-enriched envelopes would be a natural consequence.

The observed upper limit presented here implies that either the gas disk has not fully transitioned to $C/O \rightarrow 1$ at the time that the planet undergoes runaway accretion or the planet’s gas envelope is subsequently strongly polluted by the late accretion of leftover planetesimals. Alternatively, most of the metals in the gaseous envelope may be delivered before the planet undergoes runaway accretion. In van Boekel et al., (2015, in preparation), we find that the core of a giant planet can acquire a gaseous envelope well before the onset of runaway gas accretion. Once this envelope is sufficiently thick for infalling planetesimals to evaporate before reaching the planet’s core, the planet’s core stops growing and any accreted plan-

etesimals contribute to the growth of a metal-rich gas envelope. Runaway accretion of metal-poor protoplanetary gas will eventually dilute this initial envelope with vast amount of H/He; however, in this scenario the metal composition would be more representative of the solids in the protoplanetary disk than of the gas. A metal composition representative of the solids in the protoplanetary disk would naturally explain a low C/O ratio.

Finally, the observed upper limit on the C/O ratio rules out any scenario in which the planet forms inside the water snowline and accretes refractory and volatile materials with ISM-like carbon abundances (van Boekel et al., 2015, in preparation). Such scenarios would lead to $C/O > 1$, which is not in agreement with the findings presented here. Formation within the water ice line remains possible, though, if the refractory and volatile materials are oxygen-rich similar to refractory and ices materials in the Solar System.

5.2. Future Work

Observations with wider spectral coverage or substantially more precision and spectral resolution are needed to place stringent constraints on the C/O ratios in hot Jupiter gas envelopes. Despite the limitations of the current data, I was able to place a stringent upper limit of 0.9 on the C/O ratios of studied atmospheres due to the presence of detectable water absorption in their transmission spectra. In the future, the best way of also providing lower limits on the C/O ratios is to also detect the absorption of carbon-bearing species such as CO and CH_4 . Transmission spectra, in particular, provide a straightforward way of determining the relative abundances of H_2O , CO, and CH_4 by comparing the relative transit depths in the molecular absorption bands of these molecules (Benneke & Seager 2012). In this case, the SCARLET model can directly deliver the C/O ratio from observations covering near-infrared H_2O and CO or CH_4 absorption bands.

On the planet formation theory side, it will be essential to understand whether the elemental compositions of giant planet envelopes are predominately set by gas phase accretion (Öberg et al. 2011; Helling et al. 2014) or by accretion of solid and ices in the form of planetesimals (van Boekel et al., 2015 in preparation). For that, it will be crucial to understand the relative time scales for accretion of an initial gas envelope and planetesimals as well as the initialization of the gas runaway accretion. It will also be critical to understand from modeling whether the elemental composition at the bottom of my modeling domain at 1000 bars is representative of the entire gas envelope or whether the initial formation of a metal rich atmosphere and subsequent runaway gas accretion can lead to incompletely mixed, stratified gas envelopes.

Eventually, exoplanet observations may provide a statistical sample of precise C/O ratios in giant planet envelopes ranging from hot Jupiter to wide separation directly imaged giant planets. The Juno mission — expected to arrive in 2016 — will obtain the first reliable C/O measurement of for Jupiter. Meanwhile, disk observation may provide a better understanding of the elemental abundances in the protoplanetary gas and dust/ices. Together, observations of protoplanetary disks and evolved planets provide the initial conditions as well as outcome of planet formation, providing us with the

unique opportunity to develop a consistent picture of the formation of giant planets.

6. ACKNOWLEDGEMENTS

I would particularly like to thank Julie Moses for valuable discussions on photochemistry and providing me access to her chemical reactions list and detailed model outputs for model comparison and validation. I would like to

thank Caroline Morley, Mark Marley, and Jonathan Fortney for providing me with detailed information of their atmospheric models which enables me with the opportunity to compare and validate the SCARLET forward model. I thank Heather Knutson for valuable feedback on the manuscript.

APPENDIX

EFFICIENT COMPUTATION OF LINE-BY-LINE RADIATIVE-CONVECTIVE EQUILIBRIUM

Converging to radiative-convective equilibrium generally requires thousands of radiative transfer calculations of the entire atmospheric column; hence previous models have either approximated the T-p profiles based on analytical solution for (semi-)gray opacities (Guillot 2010; Parmentier & Guillot 2014) or by assuming correlated opacities across the entire atmospheric column (Burrows et al. 1997; Marley et al. 2002; Fortney et al. 2008; Morley et al. 2013). Here, I present a novel numerical technique to speed up repeated line-by-line radiative transfer calculations by orders of magnitudes — enabling the efficient computation of self-consistent T-p profiles for any atmospheric composition based on line-by-line equivalent radiative transfer. The key element of the new numerical technique is a three-dimensional radiative-connectivity array, L , describing the radiative link between any two layers in the atmosphere as a function of wavelengths. Once L is computed the T-p profile is computed using only a few hundred of spectral points, with virtually no loss in the precision compared to the full high-resolution line-by-line radiative calculations with millions of spectral points.

The basic concept of any radiative-convective model is to iterate the T-p profile until the radiative downward flux F^\downarrow due to direct star light and infrared reemission is matched by the upward emission flux in the atmosphere. In the process, atmospheric layers with temperature gradients exceeding the adiabatic lapse rate $-\frac{dT}{dz} > \Gamma = \frac{g}{C_p}$ are declared convective and adjusted to the adiabatic lapse rate. For purely absorbing atmospheres, the exact downward and upward fluxes are

$$F_i^\downarrow(\tau_i) = \int_0^\infty F_{*,\lambda} e^{-\tau_i/\mu} d\lambda + \int_0^\infty \int_0^\tau \pi B_\lambda(\tau) \frac{d}{d\tau} T_\lambda^f(\tau_i - \tau) d\tau d\lambda \quad (\text{A1})$$

$$F_i^\uparrow(\tau_i) = \int_0^\infty \pi B_\lambda(\tau_*) T_\lambda^f(\tau_* - \tau_i) d\lambda + \int_0^\infty \int_{\tau_*}^\tau \pi B_\lambda(\tau) \frac{d}{d\tau} T_\lambda^f(\tau_i - \tau) d\tau d\lambda \quad (\text{A2})$$

where the optical depth τ_i is the vertical coordinate, τ^* is the optical depth of the planet's surface, $B_\lambda(\tau)$ is the Planck function at wavelength λ for the atmospheric temperature at optical depth τ , and $F_{*,\lambda}$ is the stellar irradiation at the top of the atmosphere. The term $T_\lambda^f(\tau_i - \tau)$ is the slab transmittance

$$T_\lambda^f(\tau_i - \tau) = 2 \int_0^1 e^{-(\tau_i - \tau)/\mu} \mu d\mu \quad (\text{A3})$$

between τ_i and τ , where $\mu = \cos\theta$ is the cosine of the inclination towards the upward normal. Conceptually, the two terms in Equations A1 are the contribution from direct stellar irradiation (1st term) and the downward infrared emission from atmospheric layers above τ (2nd term). The upwards flux (Equation A2) is composed of the infrared emission from the planetary surface or deep interior (1st term) and the infrared emission from the atmospheric layers below τ_i . Iterating towards convergence, i.e. $F^\downarrow(\tau_i) = F^\uparrow(\tau_i)$ for all τ_i , is computationally extremely costly because each iteration towards convergence requires the evaluation of the double integrals in Equations A1 and A2, where capturing the high-frequency variations in the molecular line opacities requires millions of spectral points.

The key concept of the new line-by-line radiative-convective model is to break the wavelength integration into parts for which the smoothly varying Planck function, $B_\lambda(\tau)$, is approximate constant, pulling $B_\lambda(\tau)$ out of the wavelength integrals, and storing the piecewise integrated transmission terms in a three-dimensional radiative-connectivity array, L , that can be reused for many iterations till the converged temperature pressure profile is obtained.

As an example, the second term in Equation A2 in discretized atmospheres is

$$F_{i,\text{IR}}^\uparrow(\tau_i) = \int_0^\infty \sum_{j=i}^N \pi B(T_j, \lambda) \left[T_\lambda^f(\tau_i - \tau_j) - T_\lambda^f(\tau_i - \tau_{j+1}) \right] d\lambda, \quad (\text{A4})$$

where the upward IR flux at level i has contributions from all layers $j = i \dots N$ below the layer i , and $B_\lambda(T_j)$ is the

Planck function at the temperature T_j in layer j . Repeated computations of Equation A4 can be accelerated by orders of magnitude by rewriting Equation A4 as

$$F_{i,\text{IR}}^\uparrow(\tau_i) = \pi \sum_{j=i}^n \sum_{k=1}^{n_k} B(T_j, \lambda_{k+1/2}) C_{ijk}, \quad (\text{A5})$$

where

$$C_{ijk} = \int_{\lambda_k}^{\lambda_{k+1}} \left[T_\lambda^f(\tau_i - \tau_j) - T_\lambda^f(\tau_i - \tau_{j+1}) \right] d\lambda. \quad (\text{A6})$$

forms the three-dimensional radiative-connectivity array, C and n_k is the number of spectral elements saved in C . Hundreds of spectral elements suffice to perform a line-by-line equivalent evaluation because $B(\lambda, T)$ varies slowly as a function of λ and no loss of information occurs by precomputing C_{ijk} . The other terms in Equations A1 and A2 can be rewritten in a similar way.

Once all elements C_{ijk} are computed, the evaluation of Equations A1 and A2 is trivial and convergence to radiative-convective equilibrium is achieved within seconds on a modern computer. Since molecular opacities are temperature dependent, C_{ijk} needs to be repeated 3-4 times, until the model atmosphere is in radiative-convective equilibrium and the opacities correspond to the final temperature profile. Overall, the convergence to radiative equilibrium of 2-3 orders of magnitude faster performing line-by-line computations at each iterative step toward radiative-convective equilibrium.

REFERENCES

- Ackerman, A. S., & Marley, M. S. 2001, *The Astrophysical Journal*, 556, 872
- Ali-Dib, M., Mousis, O., Petit, J.-M., & Lunine, J. I. 2014, *The Astrophysical Journal*, 785, 125
- Allen, M., Yung, Y. L., & Waters, J. W. 1981, *Journal of Geophysical Research: Space Physics*, 86, 3617
- Benneke, B., & Seager, S. 2012, *The Astrophysical Journal*, 753, 100
- . 2013, *The Astrophysical Journal*, 778, 153
- Borysow, A. 2002, *Astronomy and Astrophysics*, 390, 4
- Boss, A. P. 1997, *Science*, 276, 1836
- Brown, P. N., Byrne, G. D., & Hindmarsh, A. C. 1989, *SIAM J. Sci. Stat. Comput.*, 10, 1038
- Burrows, A., Hubeny, I., & Sudarsky, D. 2005, *The Astrophysical Journal*, 625, L135
- Burrows, A., & Volobuyev, M. 2003, *The Astrophysical Journal*, 583, 985
- Burrows, A., et al. 1997, *The Astrophysical Journal*, 491, 856
- Chahine, M. T. 1974, *Journal of the Atmospheric Sciences*, 31, 233
- Cowan, N. B., Machalek, P., Croll, B., Shekhtman, L. M., Burrows, A., Deming, D., Greene, T., & Hora, J. L. 2012, *The Astrophysical Journal*, 747, 82
- Crossfield, I. J. M., Barman, T., Hansen, B. M. S., Tanaka, I., & Kodama, T. 2012a, arXiv:1210.4836
- Crossfield, I. J. M., Knutson, H., Fortney, J., Showman, A. P., Cowan, N. B., & Deming, D. 2012b, *The Astrophysical Journal*, 752, 81
- Deming, D., et al. 2013, *The Astrophysical Journal*, 774, 95
- Dorschner, J., Begemann, B., Henning, T., Jaeger, C., & Mutschke, H. 1995, *Astronomy and Astrophysics*, 300, 503
- Etangs, A. L. d., Pont, F., Vidal-Madjar, A., & Sing, D. 2008, *Astronomy and Astrophysics*, 481, 4
- Evans, T. M., Aigrain, S., Gibson, N., Barstow, J. K., Amundsen, D. S., Tremblin, P., & Mourier, P. 2015, arXiv:1504.05942 [astro-ph], arXiv: 1504.05942
- Feroz, F., Hobson, M. P., & Bridges, M. 2009, *Monthly Notices of the Royal Astronomical Society*, 398, 1601
- Fortney, J. J., Ikoma, M., Nettelmann, N., Guillot, T., & Marley, M. S. 2011, *The Astrophysical Journal*, 729, 32
- Fortney, J. J., & Marley, M. S. 2005, *Proceedings of the International Astronomical Union*, 1, 145
- Fortney, J. J., Marley, M. S., Saumon, D., & Lodders, K. 2008, *The Astrophysical Journal*, 683, 1104
- Goody, R. M., & Yung, Y. L. 1995, *Atmospheric Radiation: Theoretical Basis*, 2nd edn. (Oxford University Press, USA)
- Guillot, T. 2010, *Astronomy and Astrophysics*, 520, 13
- Hanel, R. A., Conrath, B. J., Jennings, D. E., & Samuelson, R. E. 2003, *Exploration of the Solar System by Infrared Remote Sensing*, 2nd edn. (Cambridge University Press)
- Hansen, J. E., & Travis, L. D. 1974, *Space Science Reviews*, 16, 527
- Helled, R., & Schubert, G. 2009, *The Astrophysical Journal*, 697, 1256
- Helling, C., Woitke, P., Rimmer, P. B., Kamp, I., Thi, W.-F., & Meijerink, R. 2014, *Life*, 4, 142
- Hu, R., & Seager, S. 2014, *The Astrophysical Journal*, 784, 63
- Hu, R., Seager, S., & Bains, W. 2012, *The Astrophysical Journal*, 761, 166
- Huitson, C. M., et al. 2013, *Monthly Notices of the Royal Astronomical Society*, 434, 3252
- Knutson, H. A., Charbonneau, D., Noyes, R. W., Brown, T. M., & Gilliland, R. L. 2007, *The Astrophysical Journal*, 655, 564
- Kreidberg, L., et al. 2014a, *Nature*, 505, 69
- . 2014b, *The Astrophysical Journal Letters*, 793, L27
- . 2015, arXiv:1504.05586 [astro-ph], arXiv: 1504.05586
- Lavvas, P., Yelle, R. V., & Griffith, C. A. 2010, *Icarus*, 210, 832
- Lecavelier des Etangs, A., Pont, F., Vidal-Madjar, A., & Sing, D. 2008, *Astronomy and Astrophysics*, 481, L83
- Line, M. R., Zhang, X., Vasisth, G., Natraj, V., Chen, P., & Yung, Y. L. 2012, *The Astrophysical Journal*, 749, 93
- Line, M. R., et al. 2013a, *The Astrophysical Journal*, 775, 137
- . 2013b, arXiv:1304.5561
- Madhusudhan, N., Amin, M. A., & Kennedy, G. M. 2014a, arXiv:1408.3668 [astro-ph], arXiv: 1408.3668
- Madhusudhan, N., Crouzet, N., McCullough, P. R., Deming, D., & Hedges, C. 2014b, arXiv:1407.6054 [astro-ph], arXiv: 1407.6054
- Madhusudhan, N., & Seager, S. 2009, *The Astrophysical Journal*, 707, 24
- Madhusudhan, N., et al. 2011, *Nature*, 469, 64
- Mandell, A., Haynes, K., Sinukoff, E., Madhusudhan, N., Burrows, A., & Deming, D. 2013, *Exoplanet Transit Spectroscopy Using WFC3: WASP-12 b, WASP-17 b, and WASP-19 b*, arXiv e-print 1310.2949
- Marley, M. S., Seager, S., Saumon, D., Lodders, K., Ackerman, A. S., Freedman, R. S., & Fan, X. 2002, *The Astrophysical Journal*, 568, 335
- McCullough, P. R., Crouzet, N., Deming, D., & Madhusudhan, N. 2014, *The Astrophysical Journal*, 791, 55
- McKay, C. P., Pollack, J. B., & Courtin, R. 1989, *Icarus*, 80, 23
- Menou, K. 2013, arXiv:1304.6472
- Miller-Ricci, E., Seager, S., & Sasselov, D. 2009, *The Astrophysical Journal*, 690, 1056

- Morley, C. V., Fortney, J. J., Kempton, E. M.-R., Marley, M. S., Visscher, C., & Zahnle, K. 2013, *The Astrophysical Journal*, 775, 33
- Moses, J. I., Madhusudhan, N., Visscher, C., & Freedman, R. S. 2013a, *The Astrophysical Journal*, 763, 25
- Moses, J. I., et al. 2011a, *The Astrophysical Journal*, 737, 15
- , 2011b, *The Astrophysical Journal*, 737, 15
- , 2013b, *The Astrophysical Journal*, 777, 34
- Öberg, K. I., et al. 2011, *The Astrophysical Journal*, 734, 98
- Parmentier, V., & Guillot, T. 2014, *Astronomy & Astrophysics*, 562, A133
- Piskunov, N. E., Kupka, F., Ryabchikova, T. A., Weiss, W. W., & Jeffery, C. S. 1995, *Astronomy and Astrophysics Supplement Series*, 112, 525
- Pollack, J. B., Hubickyj, O., Bodenheimer, P., Lissauer, J. J., Podolak, M., & Greenzweig, Y. 1996, *Icarus*, 124, 62
- Pont, F., Sing, D. K., Gibson, N. P., Aigrain, S., Henry, G., & Husnoo, N. 2013, *Monthly Notices of the Royal Astronomical Society*, 432, 2917
- Rodgers, C. D. 2000, *Inverse Methods for Atmospheric Sounding: Theory and Practice* (Singapore: World Scientific)
- Rothman, L., et al. 2009, *Journal of Quantitative Spectroscopy and Radiative Transfer*, 110, 533
- , 2010, *Journal of Quantitative Spectroscopy and Radiative Transfer*, 111, 2139
- Seager, S., & Sasselov, D. D. 2000, *The Astrophysical Journal*, 537, 916
- Showman, A. P., Fortney, J. J., Lian, Y., Marley, M. S., Freedman, R. S., Knutson, H. A., & Charbonneau, D. 2009, *The Astrophysical Journal*, 699, 564
- Sing, D. K., et al. 2011, *Monthly Notices of the Royal Astronomical Society*, 416, 1443
- , 2013, *Monthly Notices of the Royal Astronomical Society*, 436, 2956
- Skilling, J. 2004, *AIP Conference Proceedings*, 735, 395
- Smith, W. L. 1970, *Applied Optics*, 9, 1993
- Stevenson, K. B., Bean, J. L., Madhusudhan, N., & Harrington, J. 2014, *The Astrophysical Journal*, 791, 36
- Tennyson, J., & Yurchenko, S. N. 2012, *Monthly Notices of the Royal Astronomical Society*, 425, 21
- Visscher, C., & Moses, J. I. 2011, *The Astrophysical Journal*, 738, 72
- Wakeford, H. R., et al. 2013, *Monthly Notices of the Royal Astronomical Society*, 435, 3481
- Zahnle, K., Marley, M. S., Freedman, R. S., Lodders, K., & Fortney, J. J. 2009, *The Astrophysical Journal Letters*, 701, L20